2013

Simple and Fast Reconstruction of 6 MV Radiotherapy Doses to the Whole Body

Lydia Joyce Wilson
Louisiana State University and Agricultural and Mechanical College, lydiajwilson@gmail.com

SIMPLE AND FAST RECONSTRUCTION OF 6 MV RADIOTHERAPY DOSES TO THE WHOLE BODY

A Thesis

Submitted to the Graduate Faculty of the
Louisiana State University and
Agricultural and Mechanical College
in partial fulfillment of the
requirements for the degree of
Master of Science

in

The Department of Physics

by
Lydia J Wilson
B.A., University of California, Berkeley, 2009
December 2013

Acknowledgements

I would like to thank my advisor, Dr. Wayne Newhauser, for his support and guidance throughout the course of this project. I also thank the members of my advisory committee: Drs. Rui Zhang, John Gibbons, Maurice King, and Catherine Deibel, for their assistance and time in serving on my advisory committee.

A special thanks to Drs. Chiara LaTessa and Robert Kaderka for their contribution of photon stray dose measurements, without which this project could not have been as successful as it was. Thank you to Mr. Dan Neck for his time and invaluable help with conducting measurements and Mr. David Perrin for his guidance with the gamma index analysis. I would like to thank the members of our research group and fellow students, whose help, input, and edits were invaluable: Tony Mazza, Derek Freund, Margaret Hernandez, Andy Halloran, Dr. Oleg Vassiliev, Chris Schneider, Dr. Stephen Pittman, and Melissa Lamberto.

I would also like to thank my friends and family. Their love and support has allowed me to become who I am today and helped to keep me focused and sane through my graduate studies. Finally, I'd like to thank the LSU/MBPCC medical physics program for providing me with an excellent graduate education and the environment to ensure my success.

Table of Contents

List of Tables

List of Figures

Abstract

Background: State-of-the-art radiotherapy medical records include reliable estimates of the therapeutic radiation but are known to underestimate the stray radiation exposures by 40% away from the treatment field. Most commonly, stray radiation exposures are reconstructed using empirical formulas and/or lookup tables containing machine-specific dose measurements. The purpose of this study was to develop a physics-based model to calculate exposures to the whole body of patients who receive external beam photon radiotherapy.

Methods: We developed a physics-based analytic algorithm to predict absorbed dose from therapeutic, scatter, and leakage radiation. The model includes separate terms to characterize photon production, attenuation, and scattering in the treatment unit as well as attenuation and scatter of radiation within the phantom. It was developed using measurements of total absorbed dose in a water-box phantom from a 6 MV medical linear accelerator and was validated against measured profiles in water using several clinically representative treatment fields.

Results: Our dose algorithm reproduces the measured dose profiles in water from 1.5 to 10 cm in depth and 35 cm off-axis distance. At least 90% of predicted doses agreed within 10% or 3 mm of measured absorbed doses for positions where those doses were greater than 5% of therapeutic dose, and within 2 mGy of stray dose per Gy of therapeutic dose or 10 mm of measured doses at other locations. Computation times for 10 million dose points within a phantom were less than 6.5 minutes.

Conclusions: The results suggest that it is feasible to use a physics-based model to accurately and quickly predict whole body exposures from radiation therapy. A potentially important advantage of a physics-based approach, such as the algorithm proposed in this work, is that the

model is inherently more readily adaptable to a wide variety of treatment units and treatment techniques than models based on empirical formulae or machine specific lookup-tables.

Chapter 1 Introduction and Background

1.1 General

Cancer is one of the most significant health care problems in America today. It is estimated that 1 in 2 men and women will be diagnosed with some form of cancer in their lifetime (Howlader, et al., 2009). Nearly two thirds of cancer patients will receive radiation therapy at some point in their care (Smart, 2010) and the vast majority of these radiotherapy treatments will be done with photon therapy (DeVita, Jr, Lawrence, & Rosenberg, 2008). Thus, it is expected that a very large portion of the general population will be treated with photon radiotherapy.

Most external beam photon therapy treatments today are delivered by electron linear accelerators, or linacs. Linacs impinge an electron beam upon a stopping length, high Z target, normally made of tungsten. The slowing of electrons in the target results in Bremsstrahlung photon radiation. This photon beam is then passed through a series of beam modifying devices in the treatment head to shape the beam to the desired size and intensity profile for treatment (Khan, 2010). Figure 1 is a diagram depicting the main beam shaping and modifying components in a typical linac head.

Therapeutic radiation is that which passes through all collimating apertures and typically delivers a large dose to a small volume within the patient. Smaller levels of unwanted stray radiation, however, are also incident upon the whole body. There are three main sources of stray radiation: photon leakage through the treatment head, photon scatter from the collimation system, and photon scatter within the patient. Additionally, photoneutrons are generated, mainly in the treatment head, at electron energies greater than approximately 8 MeV (Awotwi-Pratt & Spyrou, 2007; NCRP, 2005). Figure 2 is a schematic diagram showing a patient and treatment

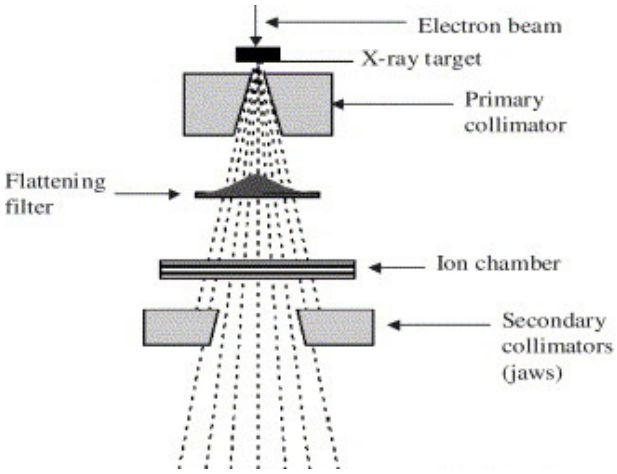

Figure 1.1 – Typical components in a medical linear accelerator head. Diagram of the components of a typical linac head for creating therapeutic photon beams (Mesbahi, Fix, Allahverdi, Grein, & Garaati, 2005).

head with the primary radiation represented in red and the blue haze depicting the bath of stray radiation to which the patient is unintentionally exposed. The dose deposited by this stray radiation can cause numerous late effects, including second malignancy. When one considers that second cancers account for approximately 15% of all cancers (Kosary, Ries, & Miller, 1995) and that it is projected that by the year 2020, there will be almost 20 million cancer survivors in the United States (de Moor, et al., 2013), a very urgent and vital need to take these out-of-field doses into account emerges.

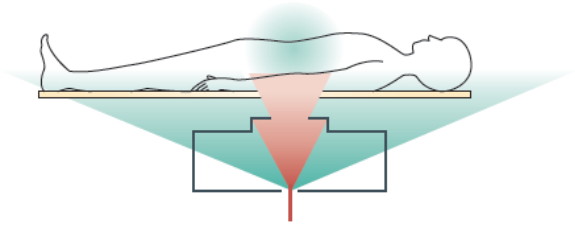

Figure 1.2 – Therapeutic and stray radiation exposures. Schematic diagram representing a linac head and patient being treated. The therapeutic radiation beam is shown in red while the blue represents the stray radiation incident upon the patient's whole body (Newhauser & Durante, 2011).

1.2 Statement of the Problem

While a lengthy and rich history of analytical dose model development exists in the literature, the majority of these studies have been devoted to developing algorithms to accurately predict the absorbed dose deposited inside of the treatment field (Johns & Cunningham, 1953; Mackie , Scrimger, & Battista, 1985; Mohan, Chi, & Lidofsky, 1986; Ahnesjo, 1989; Han, Mikell, Salehpour, & Mourtada, 2011). Despite the previously described importance of out-of-field dose consideration, comparatively fewer works have been devoted to the analytical modeling of total absorbed dose in this region (NCRP, 2009). As a result, to our knowledge, no contemporary commercial treatment planning system (TPS) includes the capability to accurately predict stray dose far from the treatment field. For example, three TPSs were recently found to be deficient in this region. Howell *et al.* (2010) found that a widely-used commercial treatment planning system (Eclipse, Varian Medical Systems, Inc., Palo Alto, CA) underestimated the out-of-field doses by an average of 40%. Additionally, the magnitude by which absorbed dose was underestimated increased with increasing distance from the treatment field. In a separate study, Joosten *et al.* (2013) compared TPS predicted doses (CMS XiO, Elekta, England) to doses calculated using Monte Carlo methods (BEAMnrc) for three different modalities of radiation therapy for breast cancer. This study found absorbed dose differences of up to 70% in out-of-field organs, even in the near-field region. We found qualitatively similar results when comparing measured doses to TPS predicted profiles (Pinnacle, Philips Healthcare, Andover, MA). Figure 1.3 shows a measured absorbed dose profile along with the corresponding TPS calculated doses. In this figure it can be seen that the TPS underestimated the absorbed dose outside of the 1% isodose line. Beyond a distance of 18 cm from the central axis (CAX), an absorbed dose of 0 mGy per Gy therapeutic dose was predicted by the TPS while the measured

absorbed dose over this region ranged from 5 mGy/Gy to 1 mGy/Gy. Thus, there is a systematic underestimation of stray radiation exposures by commonly used clinical treatment planning systems.

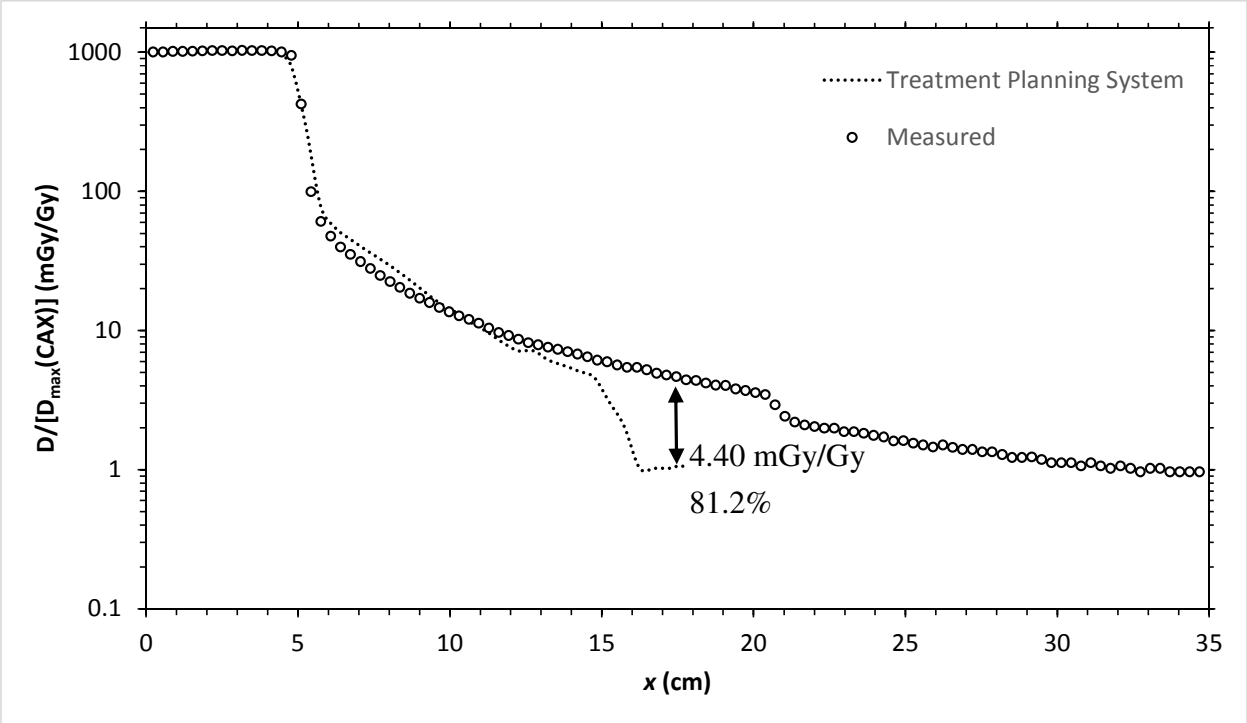

Figure 1.3 – Comparison of measured and TPS calculated dose profiles. Plot of dose profiles for a 10 x 10 cm^2 treatment field in the in-plane direction at a depth of 1.5 cm. Doses were predicted using a commercial TPS (Pinnacle, Philips Healthcare, Andover, MA).

1.3 Hypothesis and Specific Aims

In order to quickly and more accurately reconstruct radiation exposures from 6 MV photon conventional radiotherapy (CRT), we proposed a simple analytical model to calculate the absorbed dose both inside and outside of the treatment field. The hypothesis of this study is that the absorbed dose to a homogeneous water phantom from primary, leakage, and scattered radiation, from 6 MV CRT, can be accurately predicted with a physics-based analytical model (within 10% dose or 3 mm distance agreement with measured dose distributions inside of the 5% isodose line, and within 2 mGy/Gy or 10 mm agreement with measured dose distributions

outside of the 5% isodose line) for a clinically relevant interval of locations in a water-box phantom.

To test the hypothesis, we performed the following three specific aims:

Specific Aim 1: Develop and train the analytic absorbed dose model to 10% or better agreement with measured doses for square photon fields in a water-box phantom.

Specific Aim 2: Validate the analytic absorbed dose model agreement to 10% or 3 mm inside of 5%, and 2 mGy/Gy or 10 mm outside of 5% with measured absorbed doses for test cases in a water-box phantom.

Specific Aim 3: Perform uncertainty analysis, including propagation of errors to independently assess the accuracy of the absorbed dose model.

Chapter 2 Methods and Materials

This chapter presents the methods and materials used in this study. The first section overviews of the steps involved in developing the model, starting with the modeling approach (2.1.1). Next it presents formalisms for modeling the un-collimated (2.1.2) and collimated (2.1.3) photon fluences. It then describes the calculation of absorbed dose resulting from the collimated fluence in air (2.1.4) and in water (2.1.5). This is followed by the model for the un-attenuated leakage photon fluence (2.1.6) and descriptions of the absorbed dose model from leakage photons in air (2.1.7) and water (2.1.8). The virtual-source model of scattered radiation (2.1.9) is then presented along with the resulting dose in air (2.1.10) and water (2.1.11) from head-scattered photons, and that in water (2.1.12) from phantom-scattered photons. Section 2.1 also describes the data used to develop the model (2.1.13) and how empirical adjustment parameters were selected (2.1.14). Section 2.2 describes the methods of validation of the absorbed dose model against absorbed dose measurements. Finally, Section 2.3 presents methods of uncertainty analysis of the model.

2.1 Model Development

2.1.1 Analytical Model of Absorbed Dose

According to the proposed model, the total absorbed dose, D_T, to a point in a water phantom was represented as the sum of three separate components,

$$D_T = D_P + D_L + D_S\,, \tag{2.1}$$

where D_P, D_L, and D_S denoted the absorbed doses deposited by primary, leakage, and scattered photons, respectively.

The D_P and D_L components of the model depend on the model of photon fluence. The relationship between photon fluence and absorbed dose is,

$$D^{CPE} = K_c = \int \phi \times E \times \left(\frac{\mu_{en}}{\rho}\right)_{E,Z} dE = \phi \times \bar{E} \times \left(\frac{\mu_{en}}{\rho}\right)_{\bar{E},Z}, \quad 2.2$$

where D^{CPE} is the absorbed dose under conditions of charged particle equilibrium (CPE), K_c is the kinetic energy released in a medium (KERMA) due to collisional energy losses of secondary electrons, ϕ is the fluence of photons, E denotes the photon energy, $\bar{E}$ is the average photon energy of the beam, $\left(\frac{\mu_{en}}{\rho}\right)_{\bar{E},Z}$ is the mean mass energy absorption coefficient, and Z is the atomic number of the medium in which the dose is being deposited (Attix, 1986).

Charged particle equilibrium exists for depths deeper than d_{max}, except where material interfaces are present. We used measurements of total absorbed dose in a homogenous water phantom at depths equal to or deeper than d_{max} to develop the model in water. Measurements in air utilized a buildup cap of radius equal to d_{max}. Therefore, conditions of charged particle equilibrium were met in all cases studied here.

Because linac photon beams are polyenergetic, the average photon beam energy is given by,

$$\bar{E} = \frac{\int (\phi_E \times E) dE}{\int \phi_E dE}, \quad 2.3$$

where ϕ_E is the photon spectral fluence or the distribution of photons in energy and the terms E and $\bar{E}$ are as previously defined. For simplicity, we assumed a roughly triangular shape for the primary photon spectral fluence and an average photon energy equal to one-third of the peak energy (Attix, 1986). Thus, for the 6 MV photon beams studied in this paper, the average energy was estimated at 2 MeV.

Finally, values for the mean photon mass energy absorption coefficient were taken from the NIST database (Hubbell & Seltzer, 2011). Specifically,

$$\left(\frac{\mu_{en}}{\rho}\right)_{2\ MeV,air} = 2.35 \times 10^{-2}\ \mathrm{cm}^2/\mathrm{g} \quad (2.4)$$

and,

$$\left(\frac{\mu_{en}}{\rho}\right)_{2\ MeV,water} = 2.61 \times 10^{-2}\ \mathrm{cm}^2/\mathrm{g} \quad (2.5)$$

Both of these values were needed because model components for predicting D_P, and D_L were first developed in air then in water. D_S, was developed in two separate parts. The first corresponded to dose deposited by photons scattered in the treatment head, D_{HS}, which was developed first in air then in water, while the second part represented dose deposited by photons scattered in the phantom, D_{PS}, which was developed only in water.

2.1.2 Un-collimated Primary Photon Fluence

The un-collimated primary photon fluence, ϕ, is related to S, the number of photons emitted from the photon target in the treatment head. This includes photons that deposit absorbed dose from primary and leakage radiation, but not scatter radiation, which is modeled as originating elsewhere in the treatment head and phantom. In general, the total number of photons produced in the target, S, is proportional to the charge of electrons incident on the target, Q,

$$S = \kappa \times Q \ , \quad (2.6)$$

where the constant of proportionality, κ, is given by,

$$\kappa = \frac{Y(T_0) \times T_0}{\bar{E}} \times \frac{1}{e^-} \ , \quad (2.7)$$

in which the radiation yield, $Y(T_0)$, is defined to be the fraction of electron kinetic energy emitted as electromagnetic radiation (Attix, 1986), T_0 is the nominal electron beam energy, e^- is the elementary charge, and $\bar{E}$ is as was defined in Equation 2.2.

While Equation 2.6 describes the number of photons created in the target, it does not describe the spatial distribution of photons. The effective photon source, though very small, is a spatially distributed source (Svensson & Brahme, 1996). In this work, the finite lateral source size was modeled with a Gaussian function,

$$S(x) = S \times G(x, \bar{x}, \sigma), \tag{2.8}$$

where $\bar{x}$ and σ are the mean and standard deviation of that Gaussian, respectively, for the Gaussian

$$G(x, \bar{x}, \sigma) = \frac{1}{\sqrt{2\pi}\sigma} e^{-\left(\frac{(x-\bar{x})^2}{2\sigma^2}\right)}, \tag{2.9}$$

where

$$\int_{-\infty}^{\infty} G(x, \bar{x}, \sigma)\, dx = 1\,. \tag{2.10}$$

In addition to being spatially distributed, the resulting photon beam is known to produce horns at depths shallower than 10 cm in water due to the effects of the flattening filter (Khan, 2010). In order to model these horns, the un-collimated primary photon fluence was treated as a composite of three Gaussians. One Gaussian, G_1, was located on the central axis (CAX) and the other two, denoted by G_2 and G_3, were identical to one another but located symmetrically on either side of the CAX,

$$S(x) = S_1 \times G_1(x, \bar{x}_1, \sigma_1) + S_2 \times G_2(x, -\bar{x}_2, \sigma_2) + S_2 \times G_3(x, \bar{x}_2, \sigma_2). \tag{2.11}$$

In addition, empirical adjustment factors were introduced for each of these parameters, as shown in Equation 2.11, to facilitate fine tuning the model to in-air and in-water measurements as in,

$$S(x) = \sum_{i=1}^{n} S_i \times \alpha_{Q_i} \times G_i\left(x, \bar{x}_i \times \alpha_{\bar{x}_i}, \sigma_i \times \alpha_{\sigma_i}\right), \tag{2.12}$$

where n is the number of Gaussians needed to model the source, in this case 3, and α_{Q_i}, $\alpha_{\bar{x}_i}$, and α_{σ_i} are the empirical adjustment factors to the electron charge, the mean, and the width parameter of each source Gaussian, respectively. S_i is similar to S as described in Equation 2.6 but only represents the number of photons produced in each Gaussian given by,

$$S_i = \kappa \times Q_i \ , \tag{2.13}$$

where κ is as was defined in Equation 2.7 and Q_i is the number of electrons incident on the target that contribute photons to Gaussian i.

The photon fluence, $\phi(x, z)$, may be calculated according to,

$$\phi(x, z) = \sum_{i=1}^{n} S_i \times \frac{1}{4\pi[r(x, z)]^p} \ , \tag{2.14}$$

where r is the distance (Euclidean-norm) from the centroid of the source Gaussian to the point of calculation, or

$$r = \sqrt{(x - \bar{x})^2 + (z - \bar{z})^2}, \tag{2.15}$$

where $\bar{x}$ and $\bar{z}$ define the Gaussian centroid coordinates in the x and z planes, respectively. The exponent p is the parameter that describes how quickly the fluence falls off with distance from the source and is empirically found (See Section 3.1). The mean position of the source Gaussian on the z-axis, for the purposes of the calculation of r, is equal to the z-axis location of the virtual photon point source. The virtual photon source is the virtual point source from which the photon intensity appears to originate and approximately corresponds to the location of the target in the treatment head (Svensson & Brahme, 1996).

2.1.3 Collimated Primary Photon Fluence

The collimated primary photon fluence is a modification of the un-collimated primary photon fluence, representing only those photons which contribute to primary dose. This component of photon fluence was expressed as

$$\phi_P(x,z) = \sum_i^n \left[\phi_i \times G_{P,i}\left(x, \bar{x}_{P,i}(z), \sigma_{P,i}(z)\right)\right] \times C(x,z), \quad 2.16$$

where n=3, ϕ_i is from Equation 2.14, the form of $G_{P,i}\left(x, \bar{x}_{P,i}(z), \sigma_{P,i}(z)\right)$ is given by Equation 2.9, and $C(x,z)$ represents the off-axis shape caused by the black body collimation of the final field-defining aperture, which is depicted in Figure 2.1.

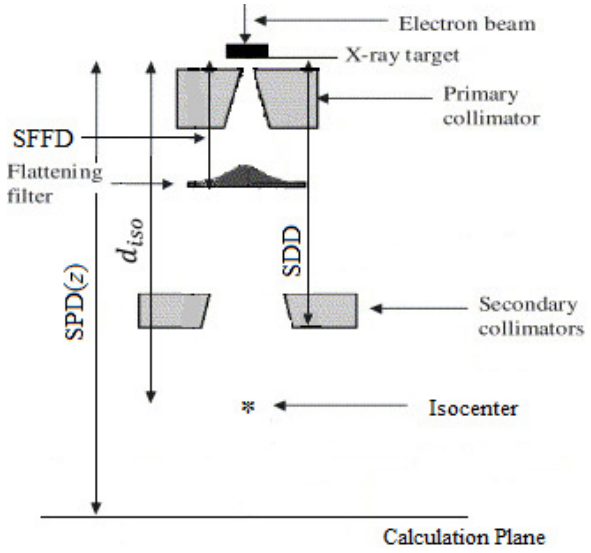

Figure 2.1 – Illustration of the photon linac head. Simplified diagram of a linac head where the secondary collimators define the final field-defining aperture. The distances involved in modeling the various absorbed dose components are also indicated.

$G_{P,i}\left(x, \bar{x}_{P,i}(z), \sigma_{P,i}(z)\right)$ is the un-collimated fluence Gaussian projected to the plane of calculation. This projection was performed from the location of the effective source to the calculation plane using similar triangles or,

$$\bar{x}_{P,i}(z) = \bar{x}_i \times \frac{d_0 + SPD(z)}{d_0} \ , \tag{2.17}$$

and,

$$\sigma_{P,i}(z) = \sigma_i \times \frac{d_0 + SPD(z)}{d_0} \ , \tag{2.18}$$

where d_0 represents the distance from the effective source to the virtual source and *SPD(z)* represents the distance from the effective source to the calculation plane. The effective source is the representation of the lateral extent of the distributed photon source which is projected with *SPD* from the location of the virtual source (Svensson & Brahme, 1996). The z-axis location of the effective source was considered to be z=0 for the coordinate system used in this study.

$C(x, z)$ models the black body absorption of primary photons by secondary collimators as shown in Figure 2.2. The penumbral shape was mathematically represented by a cumulative normal function, which is defined as the integral of a normalized Gaussian function, or

$$cnorm(x, \bar{x}, \sigma) = \frac{1}{\sqrt{2\pi}\sigma} \int_{-\infty}^{x} e^{-\left(\frac{(x-\bar{x})^2}{2\sigma^2}\right)} dx, \tag{2.19}$$

where $\bar{x}$ and σ are the mean and standard deviation of the Gaussian, respectively, and will be described by Equations 2.20-2.22, below. Based on this definition, the magnitude of the cumulative normal function ranges from 0 to 1.

The mean of this cumulative normal function in the collimated fluence model, $\bar{x}_C(z)$, is equal to the projected location of the collimator edge at the depth of calculation,

$$\bar{x}_C(z) = x_{SC} \times \frac{SPD(z)}{SDD}, \tag{2.20}$$

where x_{SC} is the physical off axis position of the secondary collimator, $SPD(z)$ was previously defined, and *SDD* is the effective source to diaphragm distance where the diaphragm, in this case, is the secondary collimator. These distances are depicted in Figures 2.1 and 2.3.

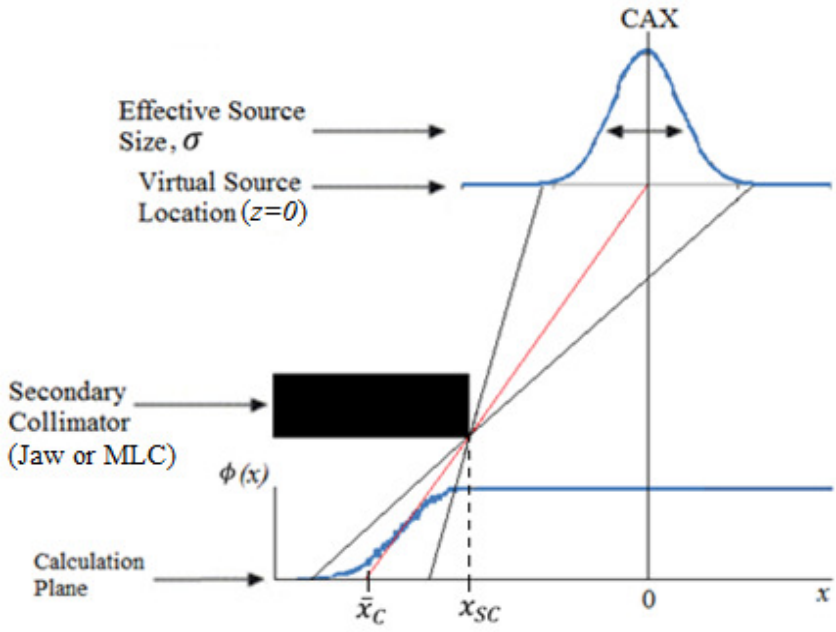

Figure 2.2 – Illustration of the black body collimation of primary photon fluence. Diagram showing the effect of black body absorption by the secondary collimator on the primary photon fluence.

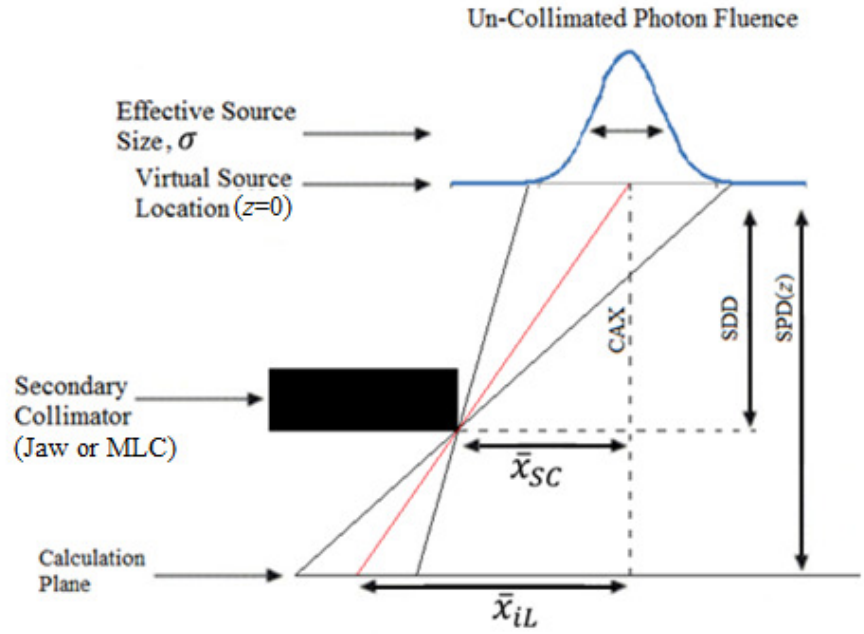

Figure 2.3 – Photon source and distances to the collimator and dose calculation point. Diagram showing the distances involved in determining the mean location and width parameter of the cumulative normal corresponding to the CAX Gaussian.

The width parameter of the primary cumulative normal corresponds to the effective source size, σ_{SRC}, and was estimated as the electron-charge-weighted average of the width parameters of the three un-collimated primary photon sources, or

$$\sigma_{SRC} = \frac{\sum_{i=1}^{n}\left[\left(\sigma_i \times \alpha_{\sigma_i} + \bar{x}_i \times \alpha_{\bar{x}_i}\right) \times Q_i \times \alpha_{Q_i}\right]}{\sum_{i=1}^{n} Q_i \times \alpha_{Q_i}} \quad 2.21$$

where σ_i, α_{σ_i}, $\bar{x}_i$, $\alpha_{\bar{x}_i}$, Q_i, and α_{Q_i} are as previously defined in Equations 2.12 and 2.13. This width parameter was then projected to the plane of calculation by similar triangles, or,

$$\sigma_{SRC}(z) = \sigma_{SRC} \times \frac{(SPD(z) - SDD)}{SDD}, \quad 2.22$$

where the distances *SPD* and *SDD* were previously defined.

The left field edge was represented by a single cumulative normal function. The right field edge, on the other hand, was represented by the complimentary cumulative normal, or,

$$ccnorm\left(x, \bar{x}_C(z), \sigma_{SRC}(z)\right) = \left(1 - cnorm\left(x, \bar{x}_C(z), \sigma_{SRC}(z)\right)\right), \quad 2.23$$

where $\bar{x}_C(z)$ and $\sigma_{SRC}(z)$ are as defined in Equations 2.20 and 2.22.

The shape of the primary photon fluence after black body absorption by the right and left collimators is then,

$$C(x,z) = cnorm\left(x, -\bar{x}_C(z), \sigma_{SRC}(z)\right) \times \left(1 - cnorm\left(x, \bar{x}_C(z), \sigma_{SRC}(z)\right)\right). \quad 2.24$$

It should be noted that for the linac with which this model was developed, the secondary collimator as indicated in Figure 2.1 was different in the in-plane and cross-plane directions. Specifically, the jaw was the secondary collimator in the in-plane direction, and the MLC served this purpose for the cross-plane direction.

2.1.4 Absorbed Dose in Air from Collimated Primary Photon Fluence

The component of the total absorbed dose deposited by the collimated primary photon fluence was modeled in air as

$$D_{P,air}^{CPE}(x,z) = \phi_P(x,z) \times \left(\frac{\mu_{en}}{\rho}\right)_{\bar{E},air} \times \bar{E}, \tag{2.25}$$

where $\phi_P(x,z)$ is the collimated primary photon fluence (Equation 2.16) and the final two terms are part of the fluence-to-dose conversion (Section 2.1.1). Substituting Equation 2.16 into Equation 2.25, we obtain

$$D_{P,air}^{CPE}(x,z) = \sum_{i}^{n} \left[\frac{S_i \times G_{P,i}(x,z)}{4\pi[r_i(x,z)]^p}\right] \times C(x,z) \times \left(\frac{\mu_{en}}{\rho}\right)_{\bar{E},air} \times \bar{E}, \tag{2.26}$$

where $r_i(x,z)$ corresponds to the Euclidean-norm between $\bar{x}_i$ and a calculation point defined by its x and z coordinates, and p is the exponent governing the divergence of the primary fluence.

2.1.5 Absorbed Dose in Water from Collimated Primary Photon Fluence

The model for absorbed dose from primary photons in water was based on the model for that in air. Specifically, the model described in Section 2.1.4 was modified to additionally take into account attenuation in water, or,

$$D_{P,w}^{CPE}(x,z) = \sum_{i=1}^{n} \left[\frac{S_i \times G_{P,i}(x,z)}{4\pi[r_i(x,z)]^p} \times TF_{i,w}(x,d)\right] \times C(x,z) \times \left(\frac{\mu_{en}}{\rho}\right)_{\bar{E},w} \times \bar{E}, \tag{2.27}$$

where $TF_{i,w}(x,d)$ is the photon transmission factor.

$TF_{i,w}(x,d)$ represents the fraction of the primary fluence incident on the water phantom that was transmitted through water to the depth of calculation. This was modeled as simple exponential attenuation of the primary photon fluence in water to the point of calculation as in,

$$TF_{i,w}(x,d) = exp[-\mu_w \cdot d_i(x) \cdot \alpha_w], \quad 2.28$$

where μ_w is the linear attenuation coefficient of water, $d_i(x)$ is the oblique depth in water, and α_w is an empirical adjustment parameter included to reduce systematic uncertainties in the estimated mean linear attenuation coefficient, the selection of which will be discussed in more detail later (See Section 2.1.14).

μ_w was determined using National Institute of Standards and Technology (NIST) data tables (Hubbell & Seltzer, 2011). These tables list attenuation coefficients for narrow beam geometry as a function of photon energy. This value was selected for the estimated mean photon energy of $\bar{E}$ = 2 MeV (See Section 2.1.1).

$d_i(x,z)$ depends on the locations of both the calculation point within the phantom and the photon source as modeled in Equation 2.12. Figure 2.4 depicts the calculation of $d_i(x)$ for an example calculation point. The corresponding angle, $\theta_i(x,z)$, was calculated by

$$\theta_i(x,z) = \tan^{-1}\frac{|x-\bar{x}_i|}{SPD(z)}, \quad 2.29$$

where $\bar{x}_i$ and *SPD(z)* are as previously defined. Using this, the oblique depth in water was calculated as,

$$d_i(x,z) = \frac{d}{\cos\theta_i(x,z)}, \quad 2.30$$

where *d* is the perpendicular depth in water of the calculation point, as depicted in Figure 2.4.

Thus far, we have treated the collimators as black body absorbers when computing fluence and dose in the primary field and penumbral regions. Next we will calculate the leakage radiation emanating from the collimators and the absorbed dose which it deposits, taking into account attenuation in these devices.

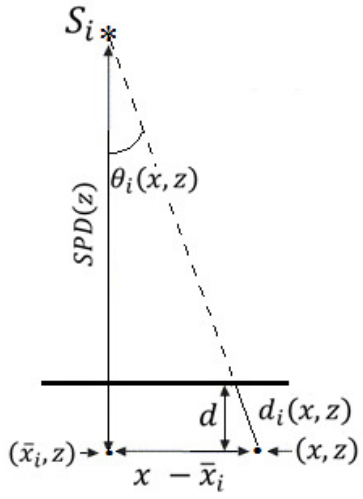

Figure 2.4 – Illustration of the oblique depth in water. Diagram depicting the oblique depth in water, d_i, and all distances involved in the calculation of this quantity.

2.1.6 Un-Attenuated Leakage Photon Fluence

The un-attenuated leakage photon fluence represents the fluence of photons contributing the leakage component of the total absorbed dose. This fluence was modeled as

$$\phi_L(x,z) = \sum_i^n \left[\phi_i \times G_{P,i}\left(x, \bar{x}_{P,i}(z), \sigma_{P,i}(z)\right)\right] \times A(x,z), \tag{2.31}$$

where n was defined in Equation 2.12, ϕ_i and $G_{P,i}\left(x, \bar{x}_{P,i}(z), \sigma_{P,i}(z)\right)$ are the same as in Equation 2.14, and $A(x,z)$ represents the percentage of photons that are transmitted through an infinitesimally thin secondary collimator as a function of *x*, as depicted in Figure 2.5. For simplicity, in our leakage model we replaced three source Gaussians with three point sources located at the mean locations of the original source Gaussians and represented by

$$\phi_L(x,z) \approx \sum_i^n [\phi_i] \times A(x,z), \tag{2.32}$$

where $A(x)$ is as before.

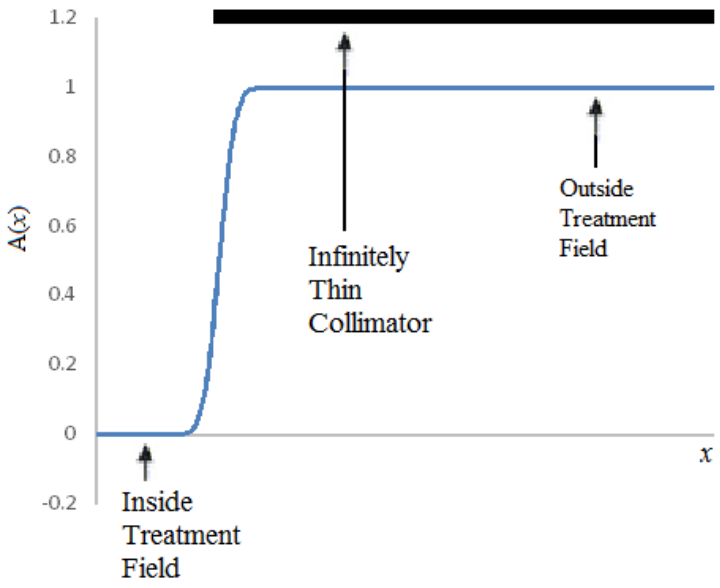

Figure 2.5 – Off-axis shape of un-attenuated leakage photon fluence, A(x). Diagram depicting the shape, $A(x)$, of the un-attenuated leakage photon fluence as resulting from an infinitely thin collimator as a function of off-axis position *x*.

In essence, $A(x,z)$ simply suppresses the leakage radiation inside the primary beam. Thus, attenuation of fluence by collimators was not yet taken into account (this will be discussed in Section 2.1.7). By definition, $A(x,z)$ has a magnitude of 0 inside the treatment field where no collimation is present, and 1 outside of the treatment field where photons reaching that calculation point from the source must traverse collimation. $A(x,z)$ was modeled with a combination of cumulative normal functions (See Equation 2.19). Thus, the model for the off-axis shape of the leakage photon fluence was given by

$$A(x,z) = \left(1 - cnorm\left(x, -\bar{x}_C(z), \sigma_{SRC}(z)\right)\right) \times cnorm\left(x, \bar{x}_C(z), \sigma_{SRC}(z)\right), \qquad 2.33$$

where $\bar{x}_C(z)$ is as was defined in Equation 2.20 and $\sigma_{SRC}(z)$ is calculated by Equation 2.22.

2.1.7 Absorbed Dose in Air from Un-Attenuated Leakage Photon Fluence

The absorbed dose deposited by the un-attenuated leakage photon fluence is known as the leakage absorbed dose. This was modeled in air as

$$D_{L,air}^{CPE}(x,z) = \sum_{i=1}^{n}\left[\phi_i \times \prod_{k=1}^{m} TF_{i,k}(x,z)\right] \times A(x) \times \left(\frac{\mu_{en}}{\rho}\right)_{\bar{E},air} \times \bar{E} \qquad 2.34$$

$$= \sum_{i=1}^{n}\left[\frac{S_i}{4\pi[r_i(x,z)]^q} \times \prod_{k=1}^{m} TF_{i,k}(x,z)\right] \times A(x) \times \left(\frac{\mu_{en}}{\rho}\right)_{\bar{E},air} \times \bar{E},$$

where n, S_i, $r_i(x,z)$, $\left(\frac{\mu_{en}}{\rho}\right)_{\bar{E},air}$, and $\bar{E}$ are defined in earlier sections (see Sections 2.1.1 and 2.1.2), and the exponent q governs the divergence of the leakage photons. The product over $k=1$ to m represents the attenuation through all m attenuating layers (e.g., jaw, MLC, primary collimator), and $TF_{i,k}(x,z)$ is the transmission factor through each layer.

$TF_{i,k}(x,z)$ is expressed differently depending on the attenuating layer. The secondary collimator may be varied to define the field size and shape to be delivered to the patient. The primary collimator, on the other hand, is a stationary collimator which is slightly larger than the largest field size the linac is capable of delivering. This means that the primary collimator is located further from the CAX than the secondary collimator for all possible field sizes. Due to these properties, the general effect of the primary and secondary collimators on the transmitted fluence is depicted in Figure 2.6.

$TF_{i,SC}(x,z)$ is the transmission factor for the secondary collimator (SC) and was calculated as

$$TF_{i,SC}(x,z) = exp\left[-\mu_{SC} \cdot t_{eff,i,SC}(x,z) \cdot \alpha_{SC}\right], \qquad 2.35$$

where μ_{SC} is the effective linear attenuation coefficient of the secondary collimator, $t_{eff,i,SC}(x,z)$ is the effective thickness of the secondary collimator for each point source, and α_{SC} is an empirical adjustment parameter to reduce the systematic uncertainty in μ_{SC}.

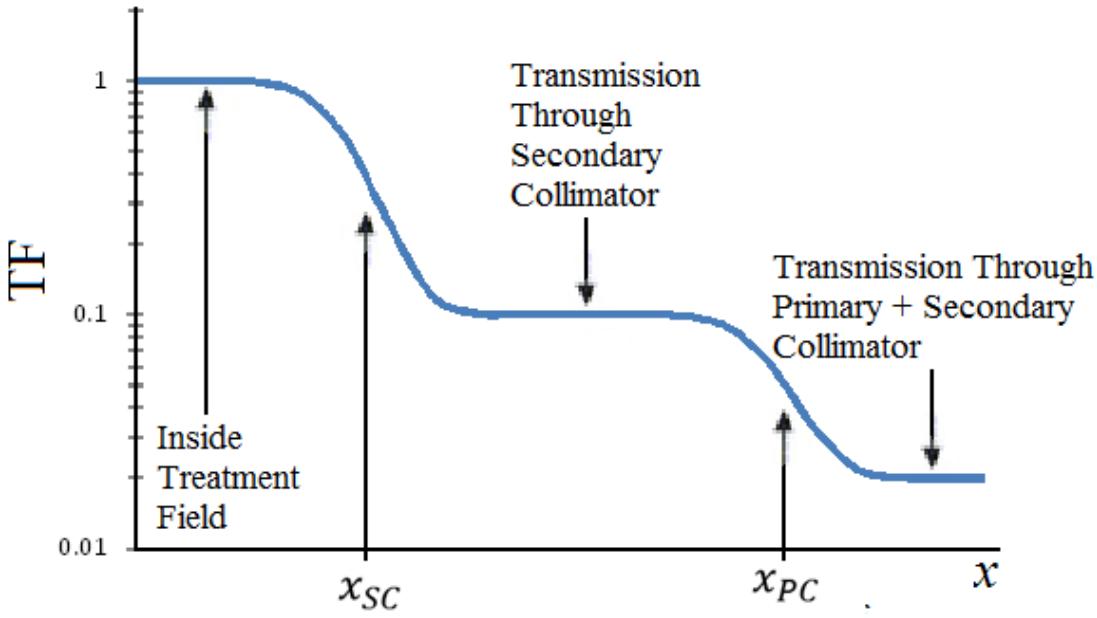

Figure 2.6 – Schematic illustration of the effect of two laterally staggered attenuating layers. Plot of $TF_{i,k}(x,z)$ after two laterally staggered attenuating layers where x_{SC} is the projected location of the secondary collimator in the plane of calculation and x_{PC} is that of the primary collimator.

$t_{eff,i,SC}(x,z)$ takes into account oblique angles using,

$$t_{eff,i,SC}(x,z) = \frac{t_{SC}}{\cos\theta_i(x,z)}\ , \tag{2.36}$$

where t_{SC} is the thickness of the secondary collimator as defined by the manufacturer and $\theta_i(x,z)$ was calculated using Equation 2.29.

It should be noted that the projected lengths of the secondary collimators for the linac used were found to extend beyond $|x| > 40$ cm, the maximum off-axis distance considered in this study. Also, the only difference in $t_{eff,i,SC}(x,z)$ for each point source is due to the different lateral mean source locations, which lead to slightly different oblique path-lengths through the collimator.

$TF_{i,PC}(x,z)$ denotes the primary collimator (PC) transmission factor and is slightly more complicated than that for the SC. The extra complexity is in part due to the fact that, unlike with

the jaws and MLCs, the effect of the PC is not present everywhere that the leakage fluence is non-zero, as was shown in Figure 2.6. Additionally, the drop in absorbed dose from attenuation in the primary collimator is characterized by a penumbral width caused by the finite effective source size. Thus, $TF_{i,PC}(x,z)$ was modeled according to,

$$TF_{i,PC}(x,z) = 1 - AF_{i,PC}(x,z) \times cnorm\big(x, \bar{x}_{PC}, \sigma_{SRC}(z) \times \alpha_{PC,\sigma}\big), \tag{2.37}$$

where $AF_{i,PC}(x,z)$ is the PC attenuation factor, $\bar{x}_{PC}$ is the projected location of the PC found using similar methods as shown by Equation 2.20, $\sigma_{SRC}(z)$ is the width parameter of the effective source projected about the PC using Equations 2.21 and 2.22, and $\alpha_{PC,\sigma}$ is an empirical adjustment factor.

$AF_{i,PC}(x,z)$ represents the fraction of incident radiation that was attenuated by the primary collimator, or

$$AF_{i,PC}(x,z) = 1 - exp\big[-\mu_{PC} \cdot t_{eff,i,PC}(x,z) \cdot \alpha_{PC}\big], \tag{2.38}$$

where μ_{pc} is the mean linear attenuation coefficient of the primary collimator, $t_{eff,i,PC}(x,z)$ is the effective thickness of the primary collimator, and α_{pc} is an empirical adjustment parameter. Unlike the secondary collimator, the primary collimator is shaped in such a way that as the off-axis position increases, the effective thickness of the collimator decreases, as shown in Figure 2.7. Thus, the effective thickness for the primary collimator was calculated as

$$t_{eff,i,PC}(x,z) = \frac{w_{PC}}{\sin\theta_i(x,z)} \ , \tag{2.39}$$

where w_{PC} is the width of the primary collimator, and $\theta_i(x,z)$ is calculated using Equation 2.29, which are both depicted in Figure 2.7.

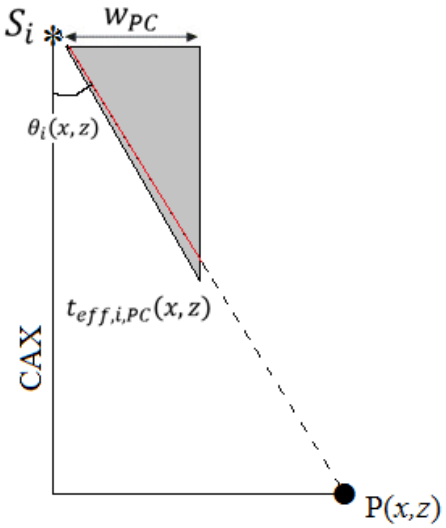

Figure 2.7 – Illustration of the primary collimator effective thickness. Diagram depicting the shape of the primary collimator and the effective thickness for an off axis calculation point *P(x,z)*.

It should be noted that linac-produced photon beams are polyenergetic; therefore, the mean linear attenuation coefficients for the secondary and primary collimators were deduced using data from NCRP Report No. 151 (2005). This was done using tenth value layers (TVLs) for lead, which are tabulated for typical linac, polyenergetic photon energy spectra. While the primary and secondary collimators of linacs are not typically made of lead, this was the material for which data were available with the closest atomic number to that of the collimators (personal communication, Elekta, Stockholm). First, a density correction was applied to the published TVL for lead in order to approximate the TVL for the specific alloy present in the collimator as in

$$TVL_k = TVL_{Pb}\frac{\rho_{Pb}}{\rho_k}\,, \tag{2.40}$$

where TVL_k and TVL_{Pb} represent the TVL of the attenuating layer material and lead, respectively, and ρ_{Pb} and ρ_k are the mass densities of lead and the attenuating layer material

(personal communication, Elekta, Stockholm), respectively. Next, the linear attenuation coefficient, μ_k, was found from the density corrected TVL using

$$\mu_k = -\frac{\ln\frac{1}{10}}{TVL_k}\ . \tag{2.41}$$

2.1.8 Absorbed Dose in Water from Un-Attenuated Leakage Photon Fluence

Up to this point the dosimetric effect of attenuation in water for leakage radiation was not modeled. This effect can be taken into account by modifying Equation 2.34 to become

$$\begin{aligned} D_{L,w}^{CPE}(x,z) &= \sum_{i=1}^{n}\left[\phi_i \times \prod_{k=1}^{m'} TF_{i,k}(x,z)\right] \times A(x) \times \left(\frac{\mu_{en}}{\rho}\right)_{\bar{E},w} \times \bar{E} \\ &= \sum_{i=1}^{n}\left[\frac{S_i}{4\pi[r_i(x,z)]^q} \times \prod_{k=1}^{m'} TF_{i,k}(x,z)\right] \times A(x) \times \left(\frac{\mu_{en}}{\rho}\right)_{\bar{E},w} \times \bar{E}, \end{aligned} \tag{2.42}$$

where $\left(\frac{\mu_{en}}{\rho}\right)_{\bar{E},w}$ was previously defined (See Section 2.1.1) and $m' = m + 1$ to allow for the transmission factor of an additional attenuating layer, i.e., water, given by $TF_{i,w}(x,d)$.

The additional transmission factor, $TF_{i,w}(x,d)$, represents the fraction of incident leakage radiation that was transmitted to the depth of the calculation point in water and is as was given by Equation 2.28.

Thus far, absorbed doses that result from those photons originating at the electron target have been considered. More specifically, scattered radiation emanating from other sources, e.g., those located elsewhere in the linac head and in the patient, have been neglected.

2.1.9 Virtual Sources of Scattered Radiation

The absorbed dose due to scattered radiation is

$$D_S = D_{HS} + D_{PS}, \tag{2.43}$$

where D_{HS} is the absorbed dose from photons scattered in the treatment head, and D_{PS} is the absorbed dose from radiation scattered in the phantom.

We modeled scatter radiation as emanating from a pair of virtual sources, as shown in Figure 2.8. These sources are separate from the source model used for primary and leakage radiations.

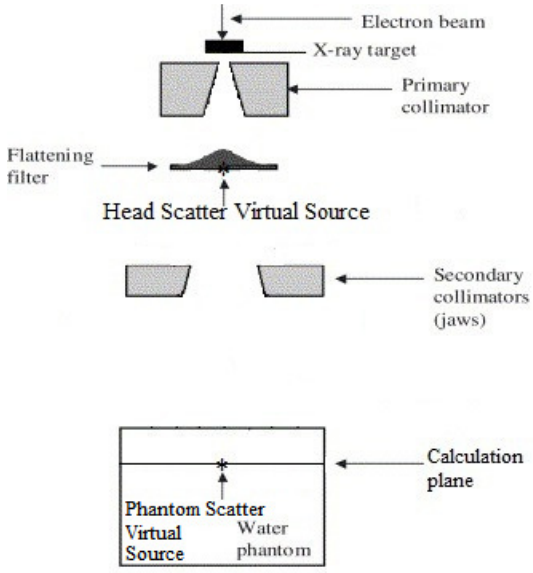

Figure 2.8 – Schematic illustration of virtual sources of scattered radiation. Diagram of the various virtual sources in the scattered dose portion of the model.

2.1.10 Absorbed Dose in Air from the Virtual Source of Head-Scattered Radiation

The virtual source of head-scattered radiation is located at the downstream edge of the flattening filter and on the CAX (McKenzie & Stevens, 1993), as shown in Figure 2.8. The absorbed dose in air from the virtual source was modeled as

$$D_{HS,air}^{CPE}(x,z) = D_{HS}(z_{FF}) \times \frac{1}{[r_{FF}(z)]^s} \times \tilde{G}_{HS}(x,z), \qquad 2.44$$

where $D_{HS}(z_{FF})$ is the head scatter reference absorbed dose magnitude defined on the CAX at the flattening filter, $r_{FF}(z)$ is the Euclidean norm between this virtual source and the calculation plane calculated using Equation 2.15, the exponent *s* governs the divergence of head-scattered

radiation, and $\tilde{G}_{HS}(x,z)$ represents the lateral Gaussian shape. Unlike the Gaussian defined in Equation 2.9, $\tilde{G}_{HS}(x,z)$ is not normalized or,

$$\tilde{G}_{HS}(x,z) = e^{-\left(\frac{(x-\bar{x})^2}{2\sigma^2(z)}\right)}, \quad 2.45$$

and thus

$$\tilde{G}_{HS}(0,z) = 1. \quad 2.46$$

$D_{HS}(z_{FF})$ is related to the size of the field incident on the phantom. As the field area increases, more of the head-scattered radiation will be able to reach the phantom. As such, this dependence was modeled as a power law, or,

$$D_{HS}(z_{FF}) = \kappa_{HS,FA} \times FA^{1/u}, \quad 2.47$$

where *FA* denotes the field area defined at the depth of calculation, the exponent *u* is a parameter governing how strongly this amplitude varies with changes in field area, and $\kappa_{HS,FA}$ is a constant of proportionality. However, this relationship is only true up to some limit. Eventually, the field size will reach a point where all of the head scatter source is visible, and $D_{HS}(z_{FF})$, the reference absorbed dose, will no longer increase with the field size. Algorithmically, this limit was,

$$FA > FA_{max} \rightarrow FA = FA_{max} \quad 2.48$$

$$FA < FA_{max} \rightarrow FA = FA \quad 2.49$$

where FA_{max} is the empirical cut-off field area defined at the depth of calculation, the selection of which will be discussed in more detail later (See Section 2.1.14).

$\tilde{G}_{HS}(x,z)$ denotes the Gaussian shape of the head scatter dose. This Gaussian is characterized by a mean located on the CAX and a width parameter at the depth of calculation of $\sigma_{HS}(z)$. The projected width parameter is,

$$\sigma_{HS}(z) = \sigma_{HS}(0) \times \frac{(SPD(z) - SFFD)}{(d_{iso} - SFFD)}, \quad 2.50$$

where $\sigma_{HS}(0)$ is the head-scatter effective source size, $SPD(z)$ has been previously defined, *SFFD* is the effective source-to-flattening-filter-distance, and d_{iso} is the distance from the effective source to isocenter, all of which are indicated in Figure 2.1. Note that the quantity in the numerator represents the distance from the virtual source to the calculation plane, while the denominator represents the virtual source to isosentric plane distance.

The width parameter of the head-scatter effective source size is related to the location of the secondary collimator and was modeled as a power law, or

$$\sigma_{HS}(0) = \kappa_{HS,\sigma} \times [x_{SC}(0)]^{1/v} \ , \tag{2.51}$$

where $x_{SC}(0)$ is the off-axis location of the secondary collimator (SC) projected to the isocentric plane, the exponent v governs how strongly the width parameter varies with lateral SC position, and $\kappa_{HS,\sigma}$ is an empirical constant of proportionality.

2.1.11 Absorbed Dose in Water from the Virtual Source of Head-Scattered Radiation

The absorbed dose in water due to head-scattered radiation was calculated according to

$$D^{CPE}_{HS,water}(x,z) = D_{HS,air}(x,z) \times TF_{HS,w}, \tag{2.52}$$

where $D_{HS,air}(x,z)$ is from equation 2.44 and $TF_{HS,w}$ is the transmission factor for head-scattered photons through water. This transmission factor was given by

$$TF_{HS,w} = exp[-\mu_w \cdot d \cdot \alpha_{HS}], \tag{2.53}$$

where μ_w is as was described in Section 2.1.5, d was defined in Equation 2.30, and α_{HS} is an adjustment parameter. $d_{FF}(x,z)$ was calculated using equation 2.30 but with all distances measured from the head scatter virtual source.

Thus far all major sources of radiation that emanate from the treatment head in some capacity have been considered. Absorbed dose from radiation that scatters in the phantom has been neglected and will be considered next.

2.1.12 Absorbed Dose in Water from the Virtual Source of Phantom-Scattered Radiation

The virtual source of phantom-scatter radiation is shown in Figure 2.8. The phantom scatter dose, by definition, only exists when a phantom is present. Thus, this portion of the model was developed exclusively for calculating dose in water. The dose due to phantom-scattered radiation was based on methods proposed by Newhauser (2011, personal communication) and used by Zhang *et al.* (2011) and Taddei *et al.* (in review). This portion of the dose was expressed as

$$D_{PS,water}^{CPE}(x,d) = D_{PS}(d)\big[C(d) \times \tilde{G}_{PS,1}(x) \times TF_{PS,1}(x) + \big(1 - C(d)\big) \times \tilde{G}_{PS,2}(x) \times TF_{PS,2}(x)\big], \quad 2.54$$

where $A_{PS}(d)$ is the integral absorbed phantom scatter dose, $C(d)$ is a partitioning factor ranging between 0 and 1 to apportion the two component Gaussians, $\tilde{G}_{PS,1}(x)$ and $\tilde{G}_{PS,2}(x)$ are each un-normalized Gaussians, and $TF_{PS,1}(x)$ and $TF_{PS,2}(x)$ are the corresponding transmission factors in water.

$A_{PS}(d)$ depends on the field area that was incident upon the phantom as well as the depth of the calculation in water. This was modeled as a power law relationship, or

$$A_{PS}(d) = \kappa_{PS,FA} \times FA(0)^{1/w} \times d^{1/b} \ , \quad 2.55$$

where $\kappa_{PS,FA}$ is an empirical constant of proportionality, $FA(0)$ is the area of the treatment field projected to the isocentric plane, the exponent *w* governs the dependence on *FA*, *d* is the perpendicular depth of the calculation plane as indicated in Figure 2.4, and the exponent *b* governs the dependence on depth.

$\tilde{G}_{PS,1}(x)$ and $\tilde{G}_{PS,2}(x)$ are the components of the total double Gaussian and follow the function detailed in Equation 2.45. The Gaussians are centered on the CAX ($\bar{x} = 0$) with width parameters $\sigma_{PS,1}$ and $\sigma_{PS,2}$, respectively.

$\tilde{G}_{PS,1}(x)$ is the narrower of the two Gaussians. The width parameter, $\sigma_{PS,1}$, was modeled as proportional to the field size as in

$$\sigma_{PS,1} = \kappa_{PS,\sigma,1} \times [x_{SC}(0)]^{1/f} \ , \tag{2.56}$$

where $\kappa_{PS,\sigma}$ is an empirical constant of proportionality, $[x_{SC}(0)]$ was defined in Equation 2.51, and the exponent *f* governs the dependence on field edge location.

$\tilde{G}_{PS,2}(x)$ represents the wider of the two Gaussians. The width parameter, $\sigma_{PS,2}$, was modeled as a function of the field area as in

$$\sigma_{PS,2} = \kappa_{PS,\sigma,2} \times FA^{1/h} \tag{2.57}$$

where $\kappa_{PS,\sigma,2}$ is an empirical constant of proportionality, FA is the area of the treatment field projected to the depth of calculation, and the exponent *h* governs the dependence on field area.

$TF_{PS,i}(x)$ models attenuation of the patient scattered radiation according to

$$TF_{PS,i} = exp\left[-\mu_w \cdot x \cdot \alpha_{PS,i}\right], \tag{2.58}$$

where μ_w was described in Section 2.1.5, *x* is the off-axis distance of the calculation point, and $\alpha_{PS,i}$ is an empirical adjustment parameter. This adjustment parameter corrects for systematic bias caused by errors in the estimation of average energy of the phantom scattered radiation. This parameter was given independent values for each phantom scatter Gaussian. By definition, one Gaussian deposits dose, on average, closer to the CAX than the other and, thus, we do not assume the average energy of photons depositing dose in each Gaussian is equal.

2.1.13 Training Data

The analytic model was trained using measured profiles of photon doses. These profiles were measured both in air and in a water-box phantom. The measurement conditions for all training data are listed in Table 2.1. Water-tank measurements used to train this model were taken from a study by Kaderka *et al.* (2012). These measurements were performed on an electron linac (Elekta SL25, Stockholm) at Universitätsklinikum (KGU) in Frankfurt, Germany operated at 6 MV. Photon doses were measured using a diamond detector (60003 PTW, Freiburg) in a water tank (PTW, Freiburg). Five lateral profiles were available (Chiarra LaTessa, personal communication, October 2012) measured in both the in-plane and cross-plane directions for two different square field sizes and at two depths in the phantom. One additional profile was measured at our institution to supplement the data from KGU as indicated in Table 2.1. In-air photon doses were measured with a farmer-type ion chamber (PTW, TN30013, S/N:0579, Freiburg) for fields produced by an electron linear accelerator (Elekta Synergy, S/N:151892, Stockholm) at Mary Bird Perkins Cancer Center in Baton Rouge, Louisiana. Measurements were recorded with all collimating apertures in their largest setting, 40x40 cm^2. Profiles were scanned in both the in- and cross-plane directions at 4 source-to-measurement-plane distances (SPDs) as well as along the CAX. In addition to this, a set of measurements was taken at the same two field sizes and SPDs as were represented in the water-tank measurements, but with the water-tank left empty.

Table 2.1 – Measurement conditions for profiles used to train the dose model. The measurement conditions for the profiles used to train the dose model are listed, including the field size, source-to-surface distance (SSD), depth, source-to-measurement-plane distance (SPD), and scan direction. The measurement conditions indicated by * represent the reference conditions selected for this study.

<table>
<tr><th colspan="5">Water-Phantom</th></tr>
<tr><th>Field Size (cm²)</th><th>SSD (cm)</th><th>Depth (cm)</th><th>Profile</th><th>Source</th></tr>
<tr><td rowspan="4">5x5</td><td rowspan="2">100</td><td rowspan="2">1.5</td><td>In-Plane</td><td rowspan="3">Kaderka et. al. (2012)</td></tr>
<tr><td>Cross-Plane</td></tr>
<tr><td rowspan="2">100</td><td rowspan="2">10</td><td>In-Plane</td></tr>
<tr><td>Cross-Plane</td><td>This Work</td></tr>
<tr><td rowspan="2">10x10 *</td><td rowspan="2">100*</td><td rowspan="2">1.5*</td><td>In-Plane</td><td rowspan="2">Kaderka et. al. (2012)</td></tr>
<tr><td>Cross-Plane</td></tr>
<tr><th colspan="5">In-Air</th></tr>
<tr><th>Field Size (cm²)</th><th colspan="2">SPD (cm)</th><th>Profile</th><th>Source</th></tr>
<tr><td rowspan="4">5x5</td><td colspan="2" rowspan="2">101.5</td><td>In-Plane</td><td rowspan="12">This Work</td></tr>
<tr><td>Cross-Plane</td></tr>
<tr><td colspan="2" rowspan="2">110</td><td>In-Plane</td></tr>
<tr><td>Cross-Plane</td></tr>
<tr><td rowspan="2">10x10 *</td><td colspan="2" rowspan="2">101.5*</td><td>In-Plane</td></tr>
<tr><td>Cross-Plane</td></tr>
<tr><td rowspan="8">40x40</td><td colspan="2" rowspan="2">85</td><td>In-Plane</td></tr>
<tr><td>Cross-Plane</td></tr>
<tr><td colspan="2" rowspan="2">100</td><td>In-Plane</td></tr>
<tr><td>Cross-Plane</td></tr>
<tr><td colspan="2" rowspan="2">115</td><td>In-Plane</td></tr>
<tr><td>Cross-Plane</td></tr>
<tr><td colspan="2" rowspan="2">130</td><td>In-Plane</td></tr>
<tr><td>Cross-Plane</td></tr>
</table>

It should be noted that the in-plane direction refers to measurements that were taken along the axis parallel to the direction of the bending magnet while cross-plane refers to measurement profiles perpendicular to the direction of the bending magnet. This naming convention is illustrated in Figure 2.9. Also, shown in this figure is the secondary collimation system in which it can be seen that the in-plane secondary collimators are located downstream of the cross-plane secondary collimators. Additionally, all data measured in this work was characterized by a much larger dose resolution than that measured by Kaderka *et al.* and thus, for

visualization purposes, all plots have been smoothed in the low dose region using a moving average filter over a range of 3 cm.

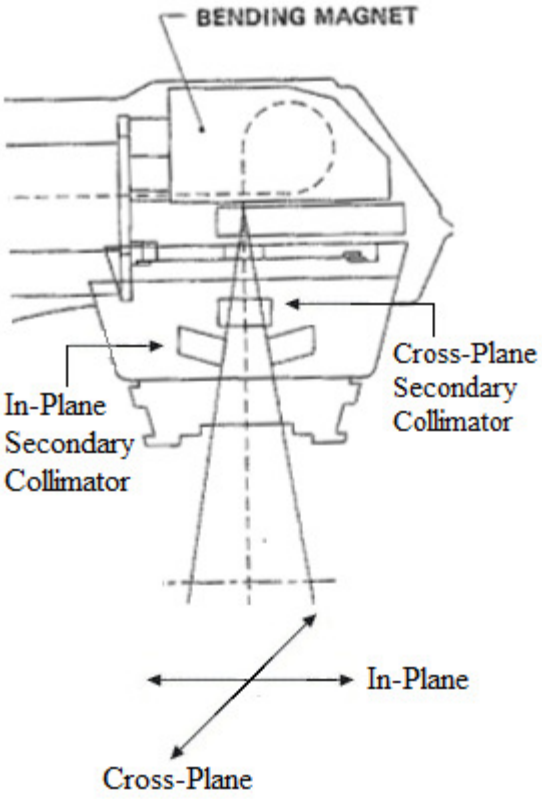

Figure 2.9 – Planar naming convention. Diagram of a general linac head and bending magnet showing the definition of in-plane and cross-plane directions.

2.1.14 Parameter Selection

Selected model parameters were determined with the use of a gradient search algorithm. This algorithm minimized the magnitude of the sum of local percent differences between measured and calculated dose values, while model parameters were allowed to vary. This algorithm was used by optimizing the local relative dose differences for groups of profiles simultaneously so that fitted parameters are applicable to multiple profiles. Once optimizations were complete, it was verified that the root mean square (RMS) local relative difference, δ_R, for each plane was $\leq 10\%$. This was calculated as

$$RMS(\delta_R) = \sqrt{\frac{1}{n}\sum_{i=1}^{n}\left[(\delta_R)_i{}^2\right]}, \tag{2.59}$$

where n is the number of data points and δ_R is the local relative difference, or

$$(\delta_R)_i = \frac{D_c(x_i) - D_m(x_i)}{D_m(x_i)}, \tag{2.60}$$

in which $D_c(x_i)$ is the calculated dose at the off-axis location x_i, and $D_m(x_i)$ is the measured dose at that same location.

The empirical parameters involved in the model for the un-collimated primary photon fluence were found by fitting to only the in-air, open field (40x40 cm^2) measured training data because this was the best approximation of an un-collimated source measurement. The mean of the central source Gaussian was assumed to be located on the CAX while all other empirical parameters were allowed to vary independently in the in-plane and cross-plane directions. This was done to allow for the possibility of a non-radially symmetric source. Additionally, the fit was done with the constraint that the magnitude of the source on the CAX must be the same in both the in-plane and cross-plane directions.

The empirical adjustment parameters for the model for absorbed dose from the collimated photon fluence as well as absorbed dose from the un-attenuated leakage fluence were found using the gradient search algorithm to simultaneously fit to all training data measured in water. Again, empirical adjustment parameters were found independently in each plane.

In order to better isolate the parameters for head-scatter absorbed dose from those for phantom-scatter absorbed dose, the empirical adjustment parameters involved in the model for absorbed dose from head-scattered radiation were found by simultaneously fitting all profiles measured in air, with the exception of the 40x40 cm^2 field data. In this way, scatter from the

phantom was excluded. One additional parameter was included specifically to calculate absorbed dose in a water-phantom from head-scattered photons, the empirical adjustment parameter to the linear attenuation coefficient of water, α_{HS}. This parameter was found by simultaneously fitting all water-phantom training data and allowing only this parameter to vary. Much like the previously-outlined portions of the model, independent values were found in the in-plane and cross-plane directions.

The empirical parameters describing dose due to phantom-scattered photons were found by simultaneously fitting all profiles measured in water. The dose due to phantom-scattered photons is most affected by the size and shape of the radiation field incident on the phantom rather than specific linac head characteristics. Thus, unlike with the previously discussed absorbed dose models, each parameter was directly applied to all data in both the in-plane and cross-plane directions and all depths. The only exception to this was for the partitioning factor, *C*. This parameter was given independent values for each depth of calculation but still shared between calculations in the in-plane and cross-plane directions.

2.2 Model Validation

2.2.1 The Gamma Index

The model was validated using an approach based on a one-dimensional gamma index analysis between measured and calculated absorbed doses. The gamma index is a convenient and widely used method to incorporate both dose difference as well as distance to agreement criteria in a single factor (Low, Harms, Mutic, & Purdy, 1998). This combination is important because large dose differences often occur in areas of steep dose gradient due to slight offsets between measured and calculated profiles.

Traditionally, the gamma index incorporates two criteria: local dose difference, ΔD, and distance to agreement, Δd. In general, the gamma index draws an ellipse around each measured data point. This ellipse is characterized by major and minor axes equal to Δd and ΔD, as depicted in Figure 2.10. The index then tests whether a calculated data point can be found within this ellipse. Due to the need to adequately validate the model in this work over a wide dynamic range of dose magnitudes, we introduced two different sets of validation criteria, specifically, for the in-field and out-of-field regions of the profiles.

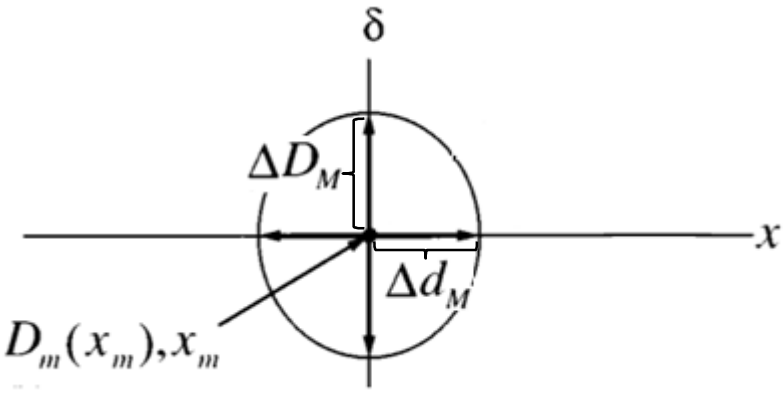

Figure 2.10 – Gamma index ellipse diagram. Illustration of a measured data point and the use of the agreement criteria, Δd and ΔD, to define an elliptical region of agreement around that data point (Low, Harms, Mutic, & Purdy, 1998).

Positions were classified as in-field or out-of-field following the methodology proposed by Howell *et al.* (2010), or

$$\frac{D_m(x_i, z)}{D_m(0, d_{max})} > 5\% \rightarrow x_i \; In - Field \tag{2.61}$$

$$\frac{D_m(x_i)}{D_m(0, d_{max})} \leq 5\% \rightarrow x_i \; Out - of - Field \tag{2.62}$$

where $D_m(x_i)$ was defined in Equation 2.60. Data points determined to be in-field were compared to a relative dose criterion, ΔD_R while out-of-field data were compared to an absolute dose criterion, D_A.

The gamma index was calculated following methods of Low *et al.* (1998). First Γ was found for every combination of measured and calculated dose values. Γ is defined as

$$\Gamma(x_m, x_c) = \sqrt{\frac{r^2(x_m, x_c)}{\Delta d^2} + \frac{\delta^2(x_m, x_c)}{\Delta D^2}} \quad , \tag{2.63}$$

where x_m and x_c are the locations of measured and calculated dose values, respectively. Note that $\Gamma(x_m, x_c)$ was found for every possible combination of measured and calculated doses and thus, $x_m \neq x_c$. The first ratio under the square root contains the distance-to-agreement (DTA) comparison where $r(x_m, x_c)$ represents the distance between the measured and calculated dose values being compared and Δd is the DTA criterion. The second ratio performs the dose difference (DD) comparison where $\delta(x_m, x_c)$ represents the DD between measured and calculated doses, and ΔD is the dose agreement criterion. Each of these values is depicted in Figure 2.11.

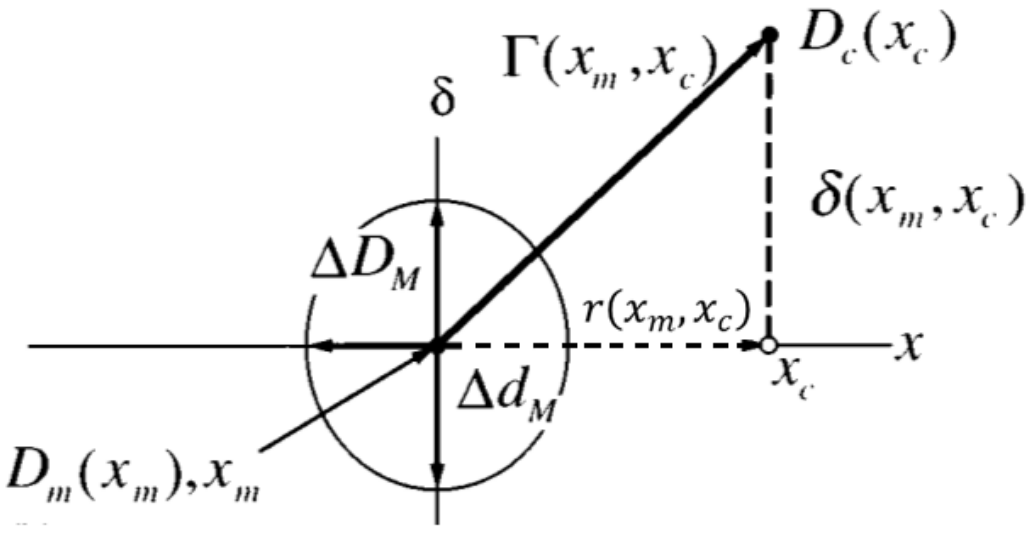

Figure 2.11 – Gamma index components. Diagram showing the various distances involved in calculating the gamma index including the distance between measured and calculated dose values, $r(x_m, x_c)$ and the dose difference between calculated and measured dose values, $\delta(x_m, x_c)$.

For all x_m determined to be in-field, a relative DD was computed as

$$\delta_R(x_m, x_c) = \frac{D_c(x_c) - D_m(x_m)}{D_m(x_m)}\ , \tag{2.64}$$

where D_c and D_m are as defined in Equation 2.60 and, x_c and x_m were defined in Equation 2.63. This relative DD value was then compared to ΔD_R.

For x_m determined to be out-of-field, the absolute DD was calculated using,

$$\delta_A(x_m, x_c) = D_c(x_c) - D_m(x_m), \tag{2.65}$$

where all parameters were defined in Equations 2.60 and 2.63. This absolute DD value was then compared to the criterion ΔD_A.

The DTA portion of this analysis remained the same for both in-field and out-of-field comparisons. More specifically,

$$r(x_m, x_c) = |x_m - x_c| \forall \{x_m\}. \tag{2.66}$$

The final gamma index array, γ, was then found by

$$\gamma(x_m) = min\{\Gamma(x_m, x_c)\} \forall \{x_c\}. \tag{2.67}$$

When found in this way, $\gamma(x_m) \leq 1$ indicates that a calculated data point was found within the ellipse characterized by ΔD and Δd drawn around $D_m(x_m)$. When this is the case, x_m is considered as passing the gamma index comparison. On the other hand, a final value of $\gamma(x_m) > 1$ indicates that a calculated dose value was not found within this ellipse and (x_m) fails. The gamma index was calculated for all validation profiles to test if the model produced a $\gamma(x_m) \leq 1$ for 90% or more of measured data points. This criterion was selected because it is the value that is in common clinical use (Nelms & Simon, 2007).

2.2.2 Validation Conditions

The ΔD_R agreement criterion was set at 10%. This value was only applied in the in-field portion of the beam, where the measured dose was greater than 5% of the dose on the CAX.

10% was selected as a goal for improving current epidemiological calculation accuracy which was reported to agree with measured doses within 20% (Stovall, et al., 2006).

ΔD_A was the absolute dose comparison criterion for the out-of-field region. This region is characterized by very low doses for which small absolute differences result in very high relative differences. ΔD_A was set at 2 mGy/Gy and was selected to be approximately twice the ionization charge quantization error in measurements in this region, which in this case was 1.08 mGy/Gy.

Figure 2.12 shows an absorbed dose profile measured in water under the reference conditions along with the upper and lower dose limits corresponding to the gamma index criteria. In this figure, all doses to the left of the dashed line are considered in the treatment field and thus, the relative criterion range is depicted. All doses to the right of this dashed line are outside of the treatment field and are surrounded by the absolute criterion interval.

Because of the vast differences in detector response between the high and low dose regions, different Δd criteria were selected for use with each of the ΔD_R and ΔD_A criteria. The Δd_R criterion was set at 3 mm because this is the value that is in common clinical use (Nelms & Simon, 2007). The criterion used for Δd_A was 10 mm. This large increase was necessary for the presence of the region of steep dose gradient due to the primary collimator in the far-from-field region where charge digitization errors were a most problematic. (Δd_A may approach the clinically used 3 mm criterion with more sensitive charge measurements). Figure 2.13 shows a measured dose profile along with the upper and lower limits based on the relative and absolute distance criteria.

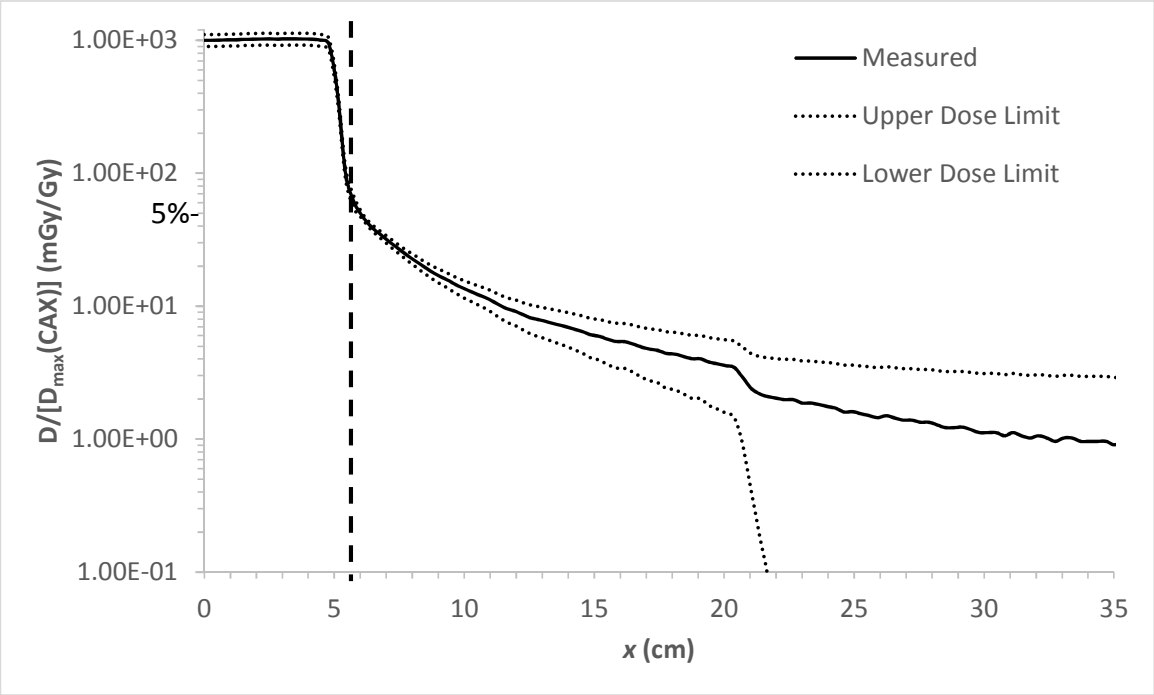

Figure 2.12 – Absolute and relative dose criteria ranges. Measured dose $\frac{D}{D_{\max(CAX)}}$ versus off-axis position x in water for a 10x10 cm^2 treatment field at a depth of 1.5 cm along with the upper and lower dose limits for both in-field and out-of-field regions.

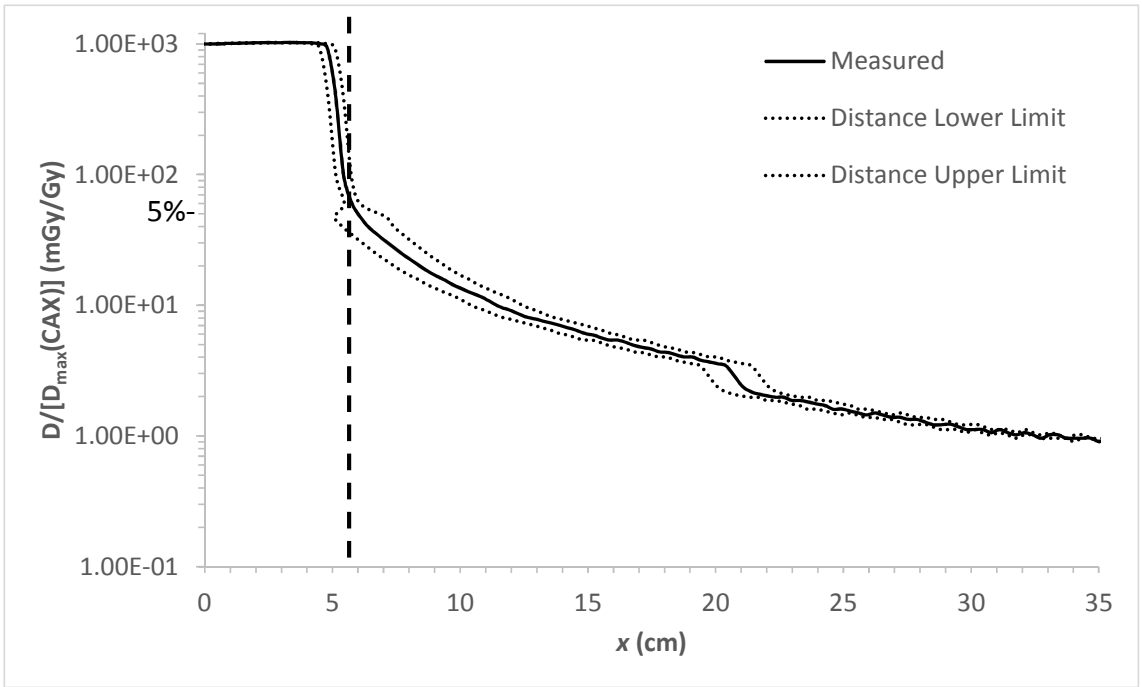

Figure 2.13 – Distance to agreement criteria intervals. Measured dose $\frac{D}{D_{\max(CAX)}}$ versus off-axis position x in water for a 10x10 cm^2 treatment field at a depth of 1.5 cm along with the upper and lower distance to agreement limits.

2.2.3 Validation Data

The model developed in Section 2.1 was validated against data measured independently of the training data. The measurement conditions for the validation data are listed in Table 2.2. Photon doses were measured both in air and in a water-tank phantom (IBA Dosimetry, Blue Phantom^2, S/N:14236, Bartlett, TN) with the use of a farmer-type ion chamber (PTW, TN30013, S/N:0579, Freiburg). Fields were produced by an electron linear accelerator at Mary Bird Perkins Cancer Center in Baton Rouge, LA, using a clinically commissioned and calibrated linac (Elekta Synergy, S/N:151892, Stockholm). Profiles in the in-plane and cross-plane directions were measured for several square and rectangular field sizes, SSDs, and depths.

To facilitate a systematic model validation, for each non-reference profile, only one characteristic was chosen to differ from the reference conditions. The cells containing # in Table 2.2 indicate that which was different from the reference conditions for each profile. It should be noted that the rectangular fields were chosen to have the same field area, *FA*, as the reference conditions but a different aspect ratio.

2.3 Uncertainty Analysis

In order to accomplish specific aim three (see Section 1.3), it was necessary to estimate the uncertainty associated with the developed dose model. This was done using standard error propagation techniques under the assumption that all model parameters were uncorrelated. More specifically, the following equation was used:

$$\sigma_f{}^2 = \left(\frac{\delta f}{\delta x}\right)^2 \sigma_x{}^2 + \left(\frac{\delta f}{\delta y}\right)^2 \sigma_y{}^2 + \left(\frac{\delta f}{\delta z}\right)^2 \sigma_z{}^2 + \cdots \qquad 2.68$$

where the notation σ_i indicates the uncertainty in the argument i and $\frac{\delta f}{\delta i}$ represents the partial derivative of f with respect to the argument i.

Table 2.2 – Measurement conditions for profiles used to validate the dose model. List of measurement conditions for profiles used to validate the dose model, including field size, aspect ratio, source-to-measurement-plane distance (SPD), source-to-surface distance (SSD), depth, and measurement direction. The reference conditions are indicated by * while those indicated with # represent those characteristics that differed from the reference conditions for each field configuration.

In-Air				
SAD (cm)	**Field Size (cm^2)**	**Aspect Ratio**	**SPD (cm)**	**Profile**
100*	10x10 *	1:1*	101.5*	In-Plane
				Cross-Plane
100	10x10	1:1	110 #	In-Plane
				Cross-Plane
100	5x20	1:4 #	101.5	In-Plane
				Cross-Plane
100	20x5	4:1 #	101.5	In-Plane
				Cross-Plane
100	20x20 #	1:1	101.5	In-Plane
				Cross-Plane
Water-Phantom				
SSD (cm)	**Field Size (cm^2)**	**Aspect Ratio**	**Depth (cm)**	**Profile**
100*	10x10*	1:1*	1.5*	In-Plane
				Cross-Plane
100	10x10	1:1	10 #	In-Plane
				Cross-Plane
100	5x20	1:4 #	1.5	In-Plane
				Cross-Plane
100	20x5	4:1 #	1.5	In-Plane
				Cross-Plane
100	20x20 #	1:1	1.5	In-Plane
				Cross-Plane
85 #	10x10	1:1	1.5	In-Plane
				Cross-Plane

For example, the uncertainty in the model for total dose as detailed in Equation 2.1 is

$$\sigma^2{}_{D_T} = \sigma^2{}_{D_P} + \sigma^2{}_{D_L} + \sigma^2{}_{D_S} \quad , \qquad 2.69$$

where the uncertainty in the total dose is equal to the quadrature sum of the uncertainties for each of the three dose components.

The uncertainty in each dose component was also found using Equation 2.68. Using this, the uncertainty in absorbed dose from the collimated primary photon fluence was found to be represented by

$$\sigma^2{}_{D_P} = \sum_i^n \left[\left(\phi_i \cdot G_{P,i} \cdot TF_{w,i} \cdot C \cdot \frac{\mu_{en}}{\rho} \cdot \sigma_{\bar{E}} \right)^2 + \left(\phi_i \cdot G_{P,i} \cdot TF_{w,i} \cdot C \cdot \bar{E} \cdot \sigma_{\frac{\mu_{en}}{\rho}} \right)^2 \right. \tag{2.70}$$

$$+ \left(\phi_i \cdot G_{P,i} \cdot TF_{w,i} \cdot \frac{\mu_{en}}{\rho} \cdot \bar{E} \cdot \sigma_C \right)^2 + \left(\phi_i \cdot G_{P,i} \cdot C \cdot \frac{\mu_{en}}{\rho} \cdot \bar{E} \cdot \sigma_{TF_{w,i}} \right)^2$$

$$\left. + \left(\phi_i \cdot TF_{w,i} \cdot C \cdot \frac{\mu_{en}}{\rho} \cdot \bar{E} \cdot \sigma_{G_{P,i}} \right)^2 + \left(G_{P,i} \cdot TF_{w,i} \cdot C \cdot \frac{\mu_{en}}{\rho} \cdot \bar{E} \cdot \sigma_{\phi_i} \right)^2 \right].$$

The uncertainty in the absorbed dose from the un-attenuated leakage fluence calculated with Equation 2.42 is similar to that for the absorbed dose from the primary fluence because both are based on the un-collimated primary photon fluence and the fluence-to-dose conversion described in Equation 2.2. The uncertainty in this component of the total dose is

$$\sigma^2{}_{D_L} = \sum_i^n \left[\left(\phi_i \cdot \prod_k^m TF_{i,k} \cdot \frac{\mu_{en}}{\rho} \cdot \bar{E} \cdot \sigma_A \right)^2 + \left(\phi_i \cdot \prod_k^m TF_{i,k} \cdot A \cdot \bar{E} \cdot \sigma_{\frac{\mu_{en}}{\rho}} \right)^2 \right. \tag{2.71}$$

$$+ \left(\phi_i \cdot \prod_k^m TF_{i,k} \cdot A \cdot \frac{\mu_{en}}{\rho} \cdot \sigma_{\bar{E}} \right)^2 + \left(\prod_k^m TF_{i,k} \cdot A \cdot \frac{\mu_{en}}{\rho} \cdot \bar{E} \cdot \sigma_{\phi_i} \right)^2$$

$$\left. + \left(\phi_i \cdot \sum_k^{m-1} TF_{i,k} \cdot A \cdot \frac{\mu_{en}}{\rho} \cdot \bar{E} \cdot \sigma_{TF_{i,m}} \right)^2 \right].$$

The scatter dose was developed in two parts, as described by Equation 2.43 and as such, the uncertainty in this component of the total dose was also derived in two parts, or

$$\sigma^2{}_{D_S} = \sigma^2{}_{D_{HS}} + \sigma^2{}_{D_{PS}} \ , \tag{2.72}$$

where σ_{HS} is the uncertainty in the absorbed dose from the head-scattered virtual source and σ_{HS} is that in the absorbed dose from the phantom-scattered virtual source. Each of these were also found using Equation 2.68 and the uncertainty in the absorbed dose from the head-scattered virtual source is

$$\begin{aligned}\sigma^2{}_{D_{HS}} = &\left(D_{HS} \cdot \frac{1}{[r_{FF}]^s} \cdot \tilde{G}_{HS} \cdot \sigma_{TF_{HS}}\right)^2 + \left(D_{HS} \cdot \frac{1}{[r_{FF}]^s} \cdot TF_{HS} \cdot \sigma_{\tilde{G}_{HS}}\right)^2 \\ &+ \left(D_{HS} \cdot \tilde{G}_{HS} \cdot TF_{HS} \cdot \frac{1}{[r_{FF}]^s} \cdot \ln r_{FF} \cdot \sigma_s\right)^2 \\ &+ \left(D_{HS} \cdot \tilde{G}_{HS} \cdot TF_{HS} \cdot -s \cdot {r_{FF}}^{-s-1} \cdot \sigma_{r_{FF}}\right)^2.\end{aligned} \tag{2.73}$$

The uncertainty in the phantom-scattered dose component is

$$\begin{aligned}\sigma^2{}_{D_{PS}} = &\left[\left(C \cdot G_{PS,1} \cdot TF_{PS,1} + (1-C) \cdot G_{PS,2} \cdot TF_{PS,2}\right) \cdot \sigma_{A_{PS}}\right]^2 \\ &+ \left[A_{PS} \cdot \left(G_{PS,1} \cdot TF_{PS,1} - G_{PS,2} \cdot TF_{PS,2}\right) \cdot \sigma_C\right]^2 \\ &+ \left(A_{PS} \cdot C \cdot TF_{PS,1} \cdot \sigma_{G_{PS,1}}\right)^2 + \left(A_{PS} \cdot C \cdot G_{PS,1} \cdot \sigma_{TF_{PS,1}}\right)^2 \\ &+ \left[A_{PS} \cdot (1-C) \cdot TF_{PS,2} \cdot \sigma_{G_{PS,2}}\right]^2 + \left[A_{PS} \cdot (1-C) \cdot G_{PS,2} \cdot \sigma_{TF_{PS,2}}\right]^2.\end{aligned} \tag{2.74}$$

The total uncertainty in calculated absorbed dose values was evaluated at four off-axis positions using the above outlined equations for the reference conditions of a 10x10 cm^2 field measured at a depth of 1.5 cm in a water-phantom with an SSD of 110 cm in both the in-plane and cross-plane directions. The four positions of interest were selected to span the entire measurement range. The four positions studied were located on the CAX, at the 5% off-axis ratio level, 15 cm from the CAX, and 30 cm from the CAX.

Chapter 3 Results

This chapter presents the results of this study. Ultimately, it details the findings for the model of total absorbed dose. First it lists the empirical parameters found to best fit the measured training data for each portion of the model (3.1). Next it shows the results of the gamma index analysis on the validation profiles (3.2). Finally, it provides the findings of the uncertainty analysis performed on calculated absorbed dose (3.3).

3.1 Model Development

3.1.1 Un-collimated Primary Photon Fluence

The un-collimated primary photon fluence was modeled as described in Section 2.1.2 and all empirical parameters were found as outlined in Section 2.1.14. The un-collimated photon fluence that best fit the measured training data in the in-plane and cross-plane directions with Equations 2.12 and 2.14 is shown in Figure 3.1. Table 3.1 summarizes the parameters involved in the calculation of this source, including the values found to yield the best fit to measured doses. From Figure 3.1 and Table 3.1 it can be seen that un-collimated fluence parameters were similar in the in-plane and cross-plane directions, with the cross-plane fluence profile being slightly wider than that in the in-plane direction. It should also be noted that all of the empirical parameters in this portion of the model correspond to physical quantities that may, in future work, be measured or estimated with the use of Monte Carlo simulations.

Figure 3.2 shows the calculated absorbed dose due to this un-collimated photon fluence for a 40x40 cm^2 treatment field, our closest approximation of an un-collimated beam, along with the corresponding measured dose profile. The secondary axis on this plot shows the local percent difference. In this plot it can be seen that the relative local dose difference is roughly

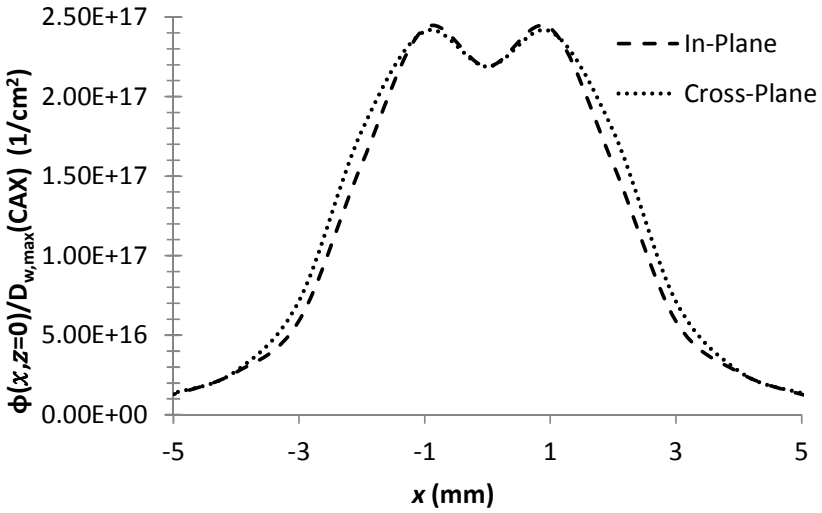

Figure 3.1 – Calculated un-collimated source of photons in the in-plane and cross-plane direction. Plot of the in-plane and cross-plane calculated un-collimated source of primary photon fluence at the location of the effective source required to deposit a dose of 1000 mGy/Gy at a depth of d_{max} in water, on the central axis.

Table 3.1 – Parameters for the un-collimated primary photon fluence.

Symbol	Description	In-Plane	Cross-Plane	Source
Q_1	Charge of electrons incident on the target contributing photons to the central Gaussian (C)	0.146	0.121	This Work[1]
Q_2	Charge of electrons incident on the target contributing photons to each peripheral Gaussian (C)	0.080	0.101	This Work[1]
σ_1	Width parameter of the central Gaussian (mm)	2.51	2.75	This Work[1]
σ_2	Width parameter of each peripheral Gaussian (mm)	0.85	0.97	This Work[1]
$\bar{x}_1$	Mean location of the central Gaussian (mm)	0		This Work[2]
$\bar{x}_2$	Off-axis mean location of each peripheral Gaussian (mm)	1.13	1.24	This work[1]
p	Exponent driving the divergence of the un-collimated photon fluence	0.97		This Work[1]
$Y(T_0)$	Photon yield for 6 MeV electrons in Tungsten	0.216		From Literature[3]

[1] From iterative fitting procedure
[2] Assumed
[3] (Attix, 1986)

constant and evenly distributed about 0. This indicates that errors are small and no significant systematic biases are present.

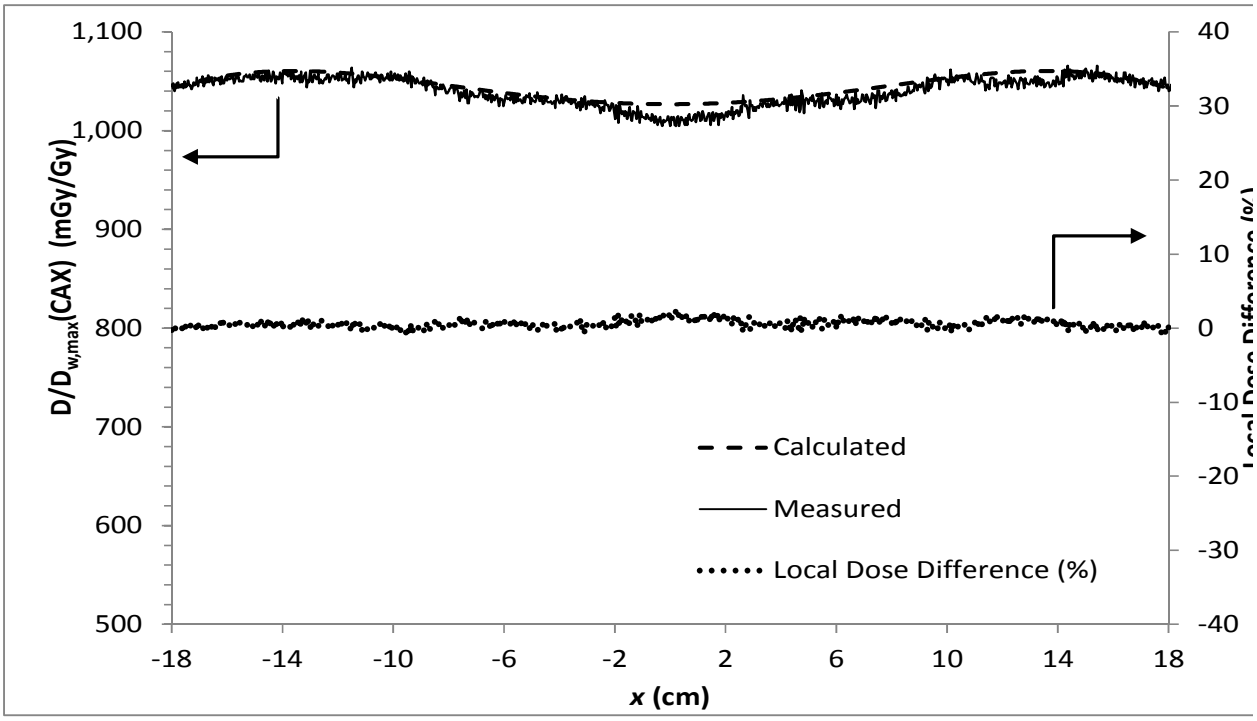

Figure 3.2 – Absorbed dose from un-collimated primary photon fluence compared to measured values. Plot showing the in-plane absorbed dose profile of a 40x40 cm^2 field, the closest possible approximation to an un-collimated source, at an SPD of 100 cm. Normalized dose profile magnitudes are indicated on the left ordinate and relative local dose differences are on the right ordinate.

3.1.2 Absorbed Dose in a Water-Phantom from Collimated Primary Photon Fluence

The absorbed dose in a water-phantom from the collimated primary photon fluence was calculated as detailed in Section 2.1.5. Figure 3.3 shows the calculated primary absorbed dose found using Equation 2.27 along with a measured total absorbed dose profile. Differences between in-plane and cross-plane measured and calculated doses were negligible for this portion of the model and thus, only in-plane profiles are shown. Table 3.2 lists all parameters involved in the calculation of the absorbed dose in water due to the collimated photon fluence.

In Figure 3.3 it can be seen that the absorbed dose due to the primary photon fluence accounts for nearly all of the dose deposited inside of the treatment field. The measured

absorbed dose profile begins to significantly deviate from the calculated absorbed primary dose around the 5% isodose line, or 50 mGy/Gy. The empirical adjustment parameters to the incident electron charge, α_{Q_i}, shown in Table 3.2 were included, and deviated from unity, because Q_i was determined from measurements which were performed in air and with a farmer-type ion chamber while the profiles to which these additional parameters were fit were measured in water with a diamond detector. Thus, we did not assume that the response of an ion chamber in air was the same as a diamond detector in water. The empirical adjustment parameters to the width parameters, α_{σ_i} were included in order to correct for any loss of spatial resolution due to the large volume of the dosimeter used to measure the in-air profiles.

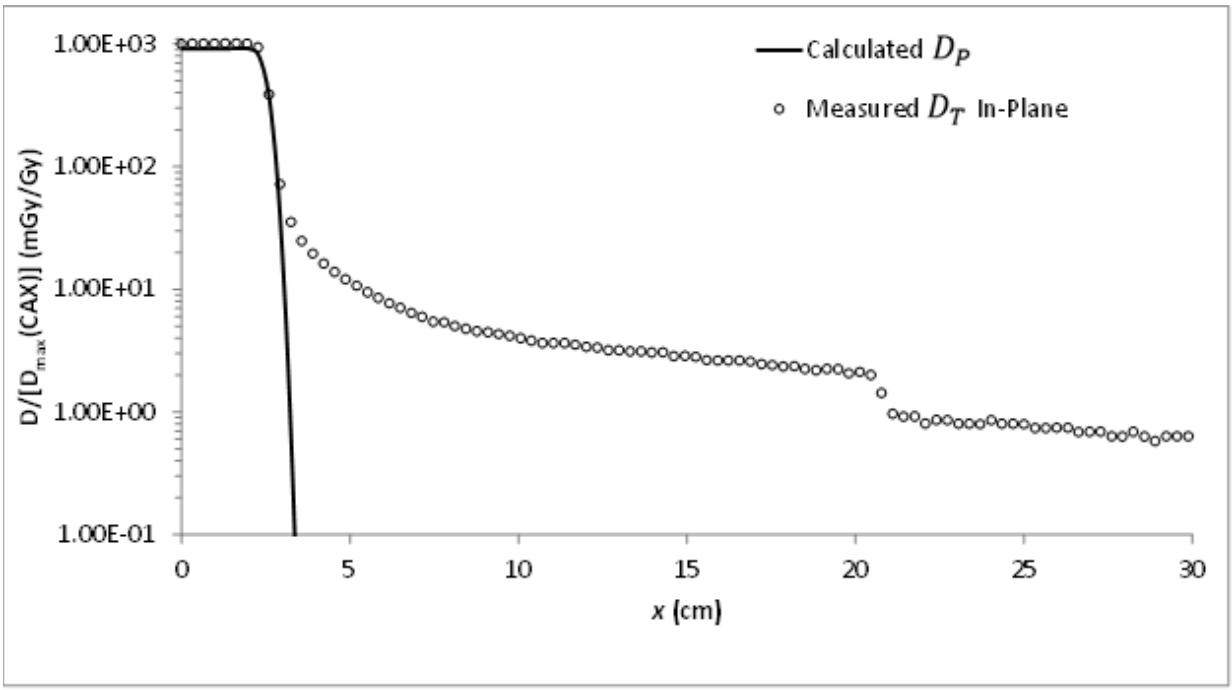

Figure 3.3 – Primary absorbed dose model in water compared to a measured total absorbed dose profile. Plot of calculated primary dose, D_P, (See Equation 2.27) shown along with an in-plane absorbed dose profile measured in water for the 5x5 cm^2 field at an SSD of 100 cm and a depth of 1.5 cm.

Table 3.2 –Parameters for the absorbed dose from primary photon fluence in water.

Symbol	Description	In-Plane	Cross-Plane	Source
α_{Q_1}	Incident electron charge empirical adjustment parameter for Gaussian 1	1.24	1.20	This Work[4]
α_{Q_2}	Incident electron charge empirical adjustment parameter for Gaussian 2	0.62	1.00	This Work[4]
α_{σ_1}	Width parameter adjustment factor for Gaussian 1	0.79	0.52	This Work[4]
α_{σ_2}	Width parameter adjustment factor for Gaussian 2	0.51	0.74	This Work[4]
$\alpha_{\bar{x}_2}$	Adjustment parameter for the mean of Gaussian 2	0.82	1.51	This Work[4]
α_w	Adjustment parameter to the μt of water	0.77		This Work[4]
d_0	Upstream distance from the effective photon source to the virtual photon source (mm)	6.03		This Work[4]
μ_w	Linear attenuation coefficient of water for 2 MeV photons (1/cm)	4.942×10^{-2}		From Literature[5]
SSD	Source-to-surface-distance (cm)	100	100	From Literature[6]
SDD	Source-to-diaphragm-distance (cm)	47	37.7	From Literature[7]

3.1.3 Absorbed Dose in a Water-Phantom from Un-Attenuated Leakage Photon Fluence

The absorbed dose in a water-phantom due to the un-attenuated leakage fluence was calculated as described in Section 2.1.8. This calculated dose component is shown for the in-plane and cross-plane directions in Figure 3.4, along with absorbed dose measured in a water-phantom for both the in-plane and cross-plane directions. Table 3.3 lists all parameters involved in the calculation of this portion of the model using Equation 2.42.

From Figure 3.4 it can easily be seen that the leakage fluence deposits the majority of the dose in the far-from-field region in both planes. Also, the magnitude of dose deposited by

[4] From iterative fitting procedure
[5] (Hubbell & Seltzer, 2011)
[6] (Kaderka, et al., 2012)
[7] (Elekta Digital Linear Accelerator User Manual, 2007)

leakage fluence is roughly equal in the in-plane and cross-plane directions at off-axis distances smaller than 20 cm and greater than 30 cm. However, the location and spread of the drop in dose due to the primary collimator is very different between the two directions. This is most likely attributable to a different average effective source location along the z axis in each the in-plane and cross-plane directions as well as different source width parameters in each direction. It should also be noted that while the absorbed dose from the collimated primary photon fluence accounted for the majority of the total absorbed dose inside the treatment field, and the absorbed dose from the leakage photon fluence gives the majority of the total absorbed dose far from the treatment field, these two portions of the model alone do not describe the absorbed dose deposited in the near-field region.

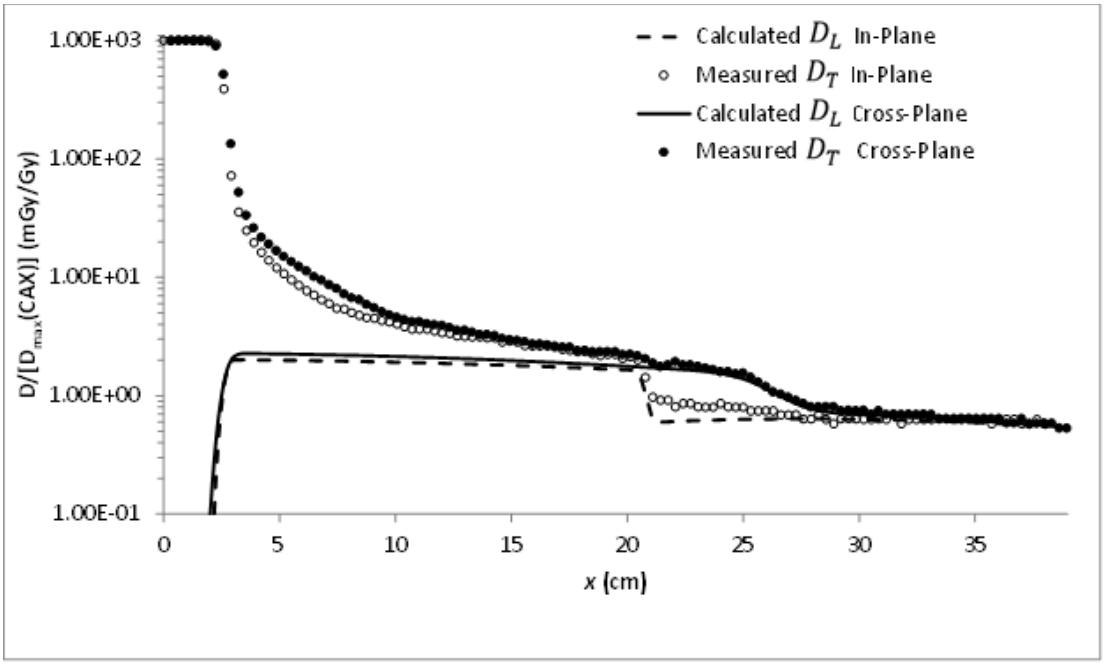

Figure 3.4 – Absorbed dose from un-attenuated leakage photon fluence compared to total absorbed dose measured in water. Plot of the calculated absorbed dose from the leakage photon fluence and measured water-tank total absorbed dose. Measured doses correspond to a 5x5 cm^2 field at an SSD of 100 cm and a measurement depth of 1.5 cm in both the in-plane and cross-plane directions.

Table 3.3 – Parameters for the absorbed dose from un-attenuated leakage photon fluence. List of all parameters involved in the calculation of absorbed dose due to the leakage photon fluence.

Symbol	Description	In-Plane	Cross-Plane	Source
$\alpha_{PC,\sigma}$	Adjustment parameter for source width for the leakage fluence attenuated by the primary collimator	0.87	4.13	This Work[8]
q	Divergence factor for the leakage photon fluence	1.58	1.11	This Work[8]
α_{SC}	Adjustment factor to the μt of the secondary collimator	1.46	1.85	This Work[8]
α_{PC}	Adjustment factor to the μt of the primary collimator	0.32	0.28	This Work[8]
SID_{PC}	Distance from the focus of the primary collimator cone to isocenter (cm)	112		This Work[8]
α_{SID}	Adjustment factor for the SID_{PC} in each plane	1.09	0.87	This Work[8]
μ_{SC}	Linear attenuation coefficient of the secondary collimator (1/cm)	0.77	0.58	From Literature[9]
t_{SC}	Secondary collimator thickness (cm)	7.8	11.2	From Literature[10]
μw_{SC}	Effective attenuation of the primary collimator	0.64		From Literature[9,10]
$\bar{x}_{PC}$	Projected location of the primary collimator in the isocentric plane (cm)	25		From Literature[10]

3.1.4 Absorbed Dose from Virtual Sources of Scattered Radiation

The absorbed dose in air from head-scattered photons was calculated as described in Section 2.1.10. Figure 3.5 shows the absorbed dose due to head-scattered photons calculated from Equation 2.44, along with total absorbed dose values measured in air. As described in Section 2.1.14, this portion of the model was first fit in air in order to better isolate the parameters for head-scatter absorbed dose from those for phantom-scatter dose. In this figure, it can be seen that the absorbed dose due to head-scattered photons is not the same in each of the

[8] From iterative fitting procedure
[9] (NCRP, NCRP Report No. 151: Structural Shielding Design and Evaluation for Megavoltage X- and Gamma-Ray Radiotherapy Facilities, 2005)
[10] Personal Communication, Elekta, Stockholm, Sweden

in-plane and cross-plane directions. The cross-plane direction was characterized by a wider Gaussian shape than the in-plane direction. This difference is reasonable considering the un-collimated photon fluence was also found to have a wider profile in the cross-plane direction than in the in-plane direction.

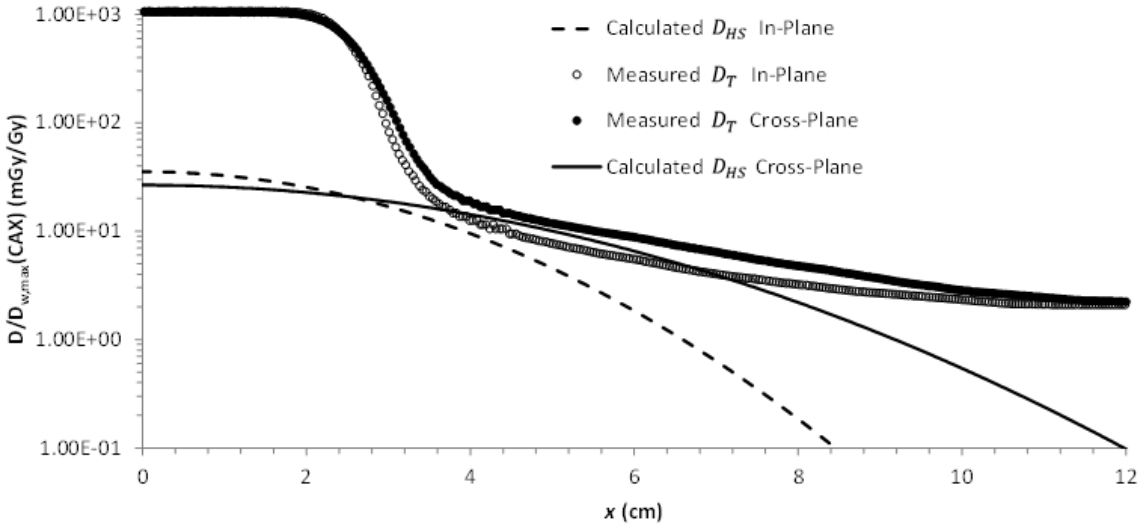

Figure 3.5 – Absorbed dose from head-scattered photons compared to in-air measured total absorbed dose profile. Plot of the calculated absorbed dose versus off-axis distance, *x*, due to head-scattered photons along with measured absorbed dose values. Measured total absorbed doses correspond to in-plane and cross-plane profiles for a 5x5 cm^2 field measured in air at an SPD of 101.5 cm.

Table 3.4 lists all parameters involved in calculating dose due to head-scattered photons in both air and water. These parameters were found following methods described in Section 2.1.14. The model parameters describing the absorbed dose due to head-scattered photons developed in air were also used in the calculation of absorbed dose in a water-phantom with Equation 2.52. Additionally, the empirical adjustment parameter to the water attenuation coeffici ent for head-scattered radiation was included in the model for dose in water. Figure 3.6 shows the absorbed dose due to head-scattered photons in a water-phantom along with measured total absorbed dose.

Table 3.4 – Parameters for the absorbed dose from head-scattered photons.

Symbol	Description	In-Plane	Cross-Plane	Source
$\kappa_{HS,FA}$	Constant of proportionality for the head-scatter Gaussian $\left(mGy \cdot Gy^{-1} \cdot mm^{-2 \cdot 1/u}\right)$	4.66×10^6	4.15×10^7	This Work[11]
u	Exponent defining power law relationship between the amplitude and field area	3.59	2.62	This Work[11]
s	Divergence factor for head-scattered absorbed dose	2.07	2.55	This Work[11]
$\kappa_{HS,\sigma}$	Constant of proportionality for the head-scatter Gaussian width parameter $\left(mm \cdot mm^{-1/v}\right)$	0.72	1.2	This Work[11]
α_{HS}	Adjustment parameter for the μt of water for head-scattered absorbed dose	1.12	2.79	This Work[11]
FA_{max}	Cut-off field area defined in the isocentric plane (cm^2)	301		This Work[11]
SFFD	Effective-source-to-flattening-filter-distance (cm)	17		From Literature[12]

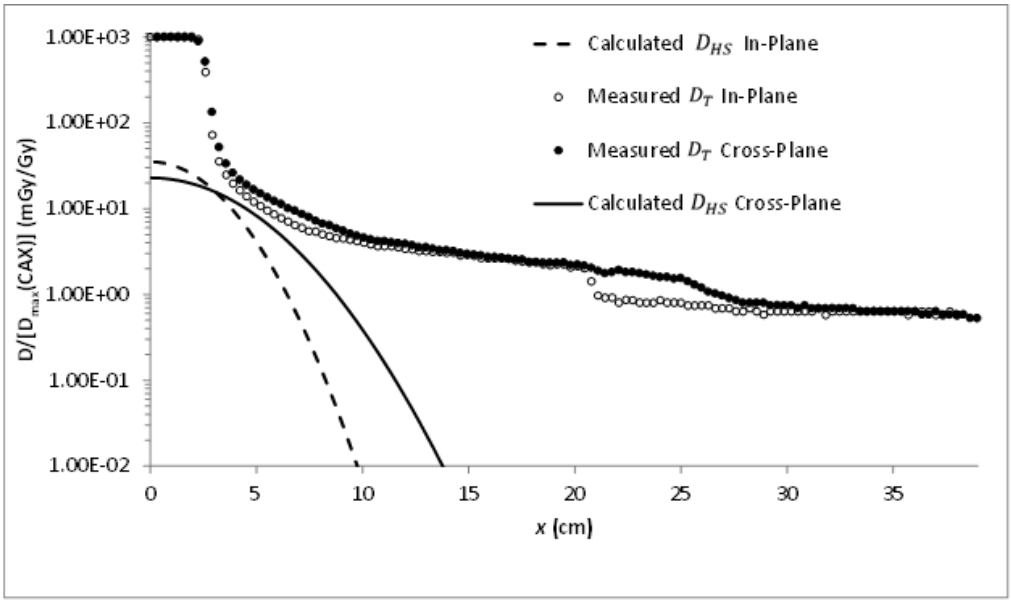

Figure 3.6 – Absorbed dose due to head-scattered photons compared to total absorbed dose profiles measured in water. Plot of calculated absorbed dose due to head-scattered radiation and total absorbed dose profiles measured in both the in-plane and cross-plane directions. Measurements represent a 5x5 cm^2 field with the water-phantom at an SSD of 100 cm and the chamber at a depth of 1.5 cm in water.

[11] From iterative fitting procedure
[12] (Elekta Digital Linear Accelerator User Manual, 2007)

In Figure 3.5 it can be seen that the dose due to head-scattered photons represents nearly all of the dose deposited in the near-field region in air. A very small contribution to the total dose in this region also comes from leakage photons. Figure 3.6, however, shows that in water, the absorbed dose from head-scattered photons represents a comparatively smaller, but still significant portion of the total dose in this region. This is because in water the phantom-scattered photons also deposit a large contribution to the total absorbed dose in this region.

Following the methodology outlined in Section 2.1.12, namely Equation 2.54, the absorbed dose due to phantom-scattered photons was calculated. Figure 3.7 shows the calculated absorbed dose from phantom-scattered photons along with water-tank measured total absorbed dose values. It should be noted that the phantom-scatter dose is modeled the same in the in-plane and cross-plane directions at each depth and thus only one calculated curve is shown in this figure. Table 3.5 lists all parameters involved in calculating this portion of the dose. In Figure 3.7 it can be seen that the absorbed dose due to phantom-scattered photons significantly contributes to the total dose in the near-field region; and it continues to deposit dose much further from the CAX than the head-scattered photons.

3.1.5 Calculated Total Absorbed Dose in a Water-Phantom

The total absorbed dose in both air and water was calculated as described in Section 2.1.1, specifically using Equation 2.1. Figure 3.8 shows each of the calculated dose components, D_P, D_L, D_{HS}, and D_{PS}, the calculated total absorbed dose, D_T, and the measured total absorbed dose profile for a representative case. Figure 3.9 shows these same measured and calculated total absorbed dose profiles along with the relative local dose deviations. In this plot, it can be seen that the largest deviations between calculated and measured dose values exist in the areas of steep dose gradients. This was expected because in these regions, small offsets between

measured and calculated dose profiles result in large relative local deviations. There also appears to be a systematic underestimation of dose just outside of the treatment field, which will be discussed in more detail later.

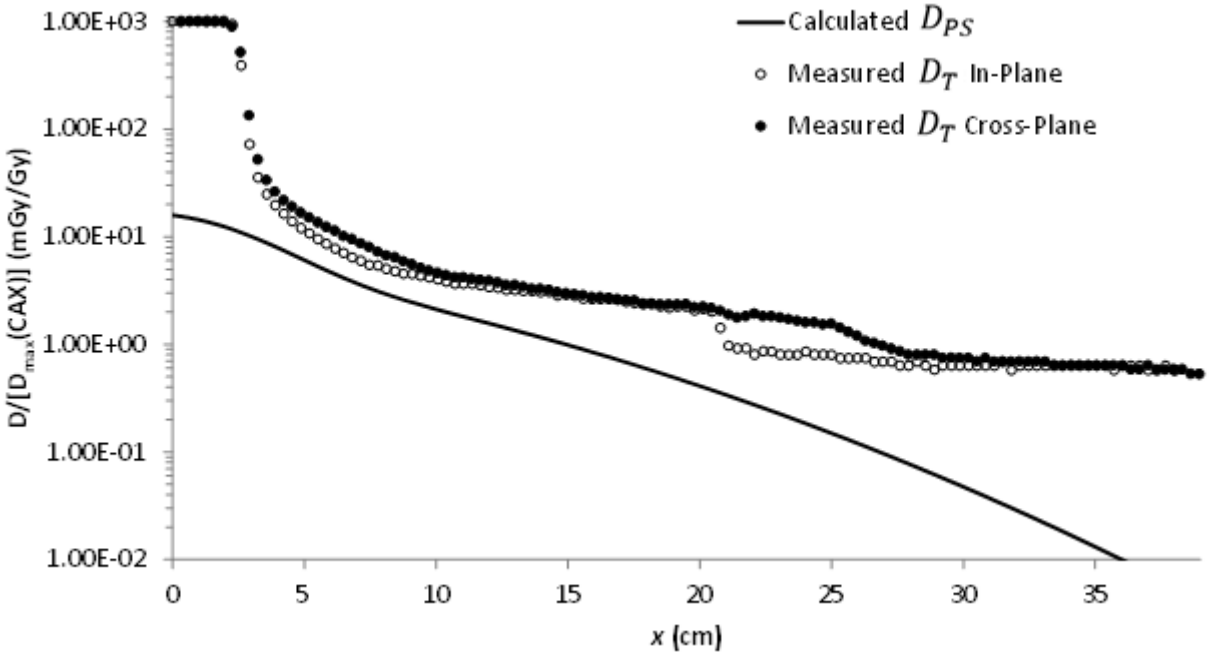

Figure 3.7 – Absorbed dose from phantom-scattered photons compared to a measured water-tank absorbed dose profile. Plot of calculated phantom-scatter absorbed dose and measured total absorbed dose values for both in-plane and cross-plane profiles. Total absorbed dose was measured for a 5x5 cm^2 field with an SSD of 100 cm and a measurement depth of 1.5 cm.

Table 3.6 lists the relative RMS deviation between calculated and measured total absorbed dose for each training profile in water. In this table, it can be seen that all but one field, the 5x5 cm^2 field measured at a depth of 10 cm in the cross-plane direction, passed the criterion stated in Specific Aim 1 (See Section 1.2) of 10% or better agreement in water. However, this is because this profile was measured for this work while all others listed in this table were measured by Kaderka *et al.* (2012). As previously mentioned, the measurements from this work had a significantly lower dose resolution than those from Kaderka *et al.*, which most seriously affected dose measurements in the far-from-field region. This is also the region where small

absolute dose differences correspond to large relative differences and thus, a very large relative RMS error.

Table 3.5 – Parameters for the absorbed dose from the phantom-scattered photons. List of parameters for the calculation of the phantom-scatter absorbed dose.

Symbol	Description	d=1.5 cm	d=10 cm	Source
κ_{FA}	Constant of proportionality for the double-Gaussian amplitude $\left(mGy \cdot Gy^{-1} \cdot mm^{-2 \cdot \frac{1}{w} \cdot \frac{1}{b}}\right)$	3.8×10^{-2}		This Work[13]
w	Exponent defining power law relationship between the amplitude and field area	1.7		This Work[13]
b	Exponent defining power law relationship between amplitude and depth	1.9		This Work[13]
$\kappa_{PS,\sigma,1}$	Constant of proportionality for the width parameter of Gaussian 1 $\left(mm \cdot mm^{\frac{-1}{f}}\right)$	12		This Work[13]
f	Exponent defining power law relationship between width parameter of Gaussian 1 and field size	3.0		This Work[13]
$\kappa_{PS,\sigma,2}$	Constant of proportionality for the width parameter of Gaussian 2 $\left(mm \cdot mm^{\frac{-1}{h}}\right)$	1.1		This Work[13]
h	Exponent defining power law relationship between width parameter of Gaussian 2 and field area	1.6		This Work[13]
C	Partitioning factor for the two Gaussians making up the phantom-scatter double-Gaussian	0.59	0.80	This Work[13]
$\alpha_{PS,1}$	Adjustment parameter to the μd of the phantom-scattered photons in Gaussian 1	1.7		This Work[13]
$\alpha_{PS,2}$	Adjustment parameter to the μd of the phantom-scattered photons in Gaussian 2	2.5		This Work[13]

[13] From iterative fitting procedure

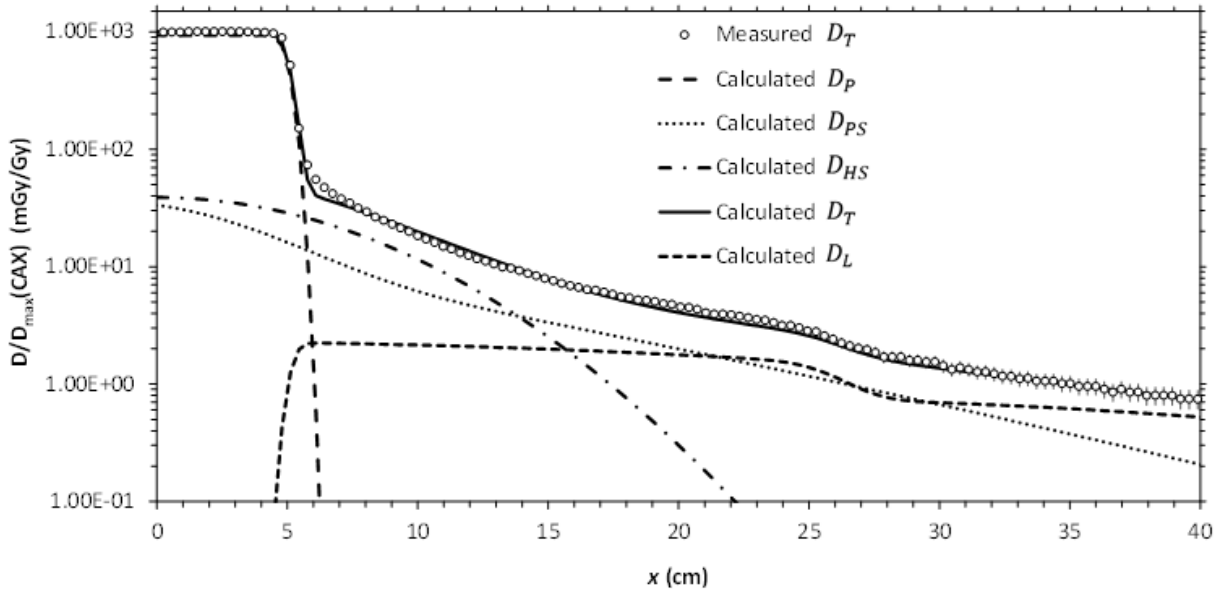

Figure 3.8 – Calculated absorbed dose components and total absorbed dose compared to a measured total absorbed dose profile in water. Plot of each of the components of the calculated total absorbed dose along with their sum and measured total absorbed dose. Doses were measured in the cross-plane direction for a 10x10 cm^2 field with an SSD of 100 cm and at a depth of 1.5 cm in water. Error bars represent one standard deviation as given by Kaderka *et al.*.

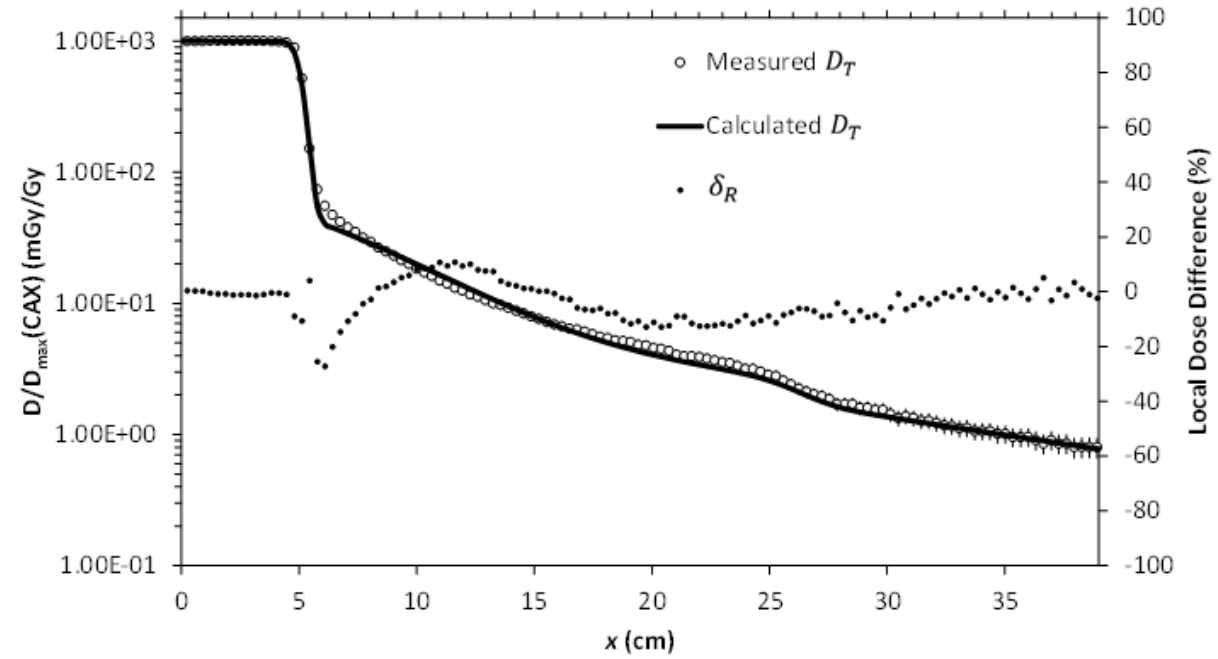

Figure 3.9 – Calculated total absorbed dose compared to measured total absorbed dose with relative local difference. Plot of the calculated total absorbed dose along with measured total absorbed doses for a 10x10 cm^2 field, SSD of 100 cm, and depth of 1.5 cm in a water-phantom in the cross-plane direction. Also, indicated on the right ordinate, is the relative local dose difference.

Table 3.6 – RMS relative local deviations between measured and calculated total absorbed dose in water.

Field Size (cm^2)	SSD (cm)	Depth (cm)	Profile	RMS
5x5	100	1.5	In-plane	7.57
			Cross-plane	5.79
	100	10	In-plane	8.22
			Cross-plane	35.81
10x10	100	1.5	In-plane	9.29
			Cross-plane	7.97
All Fields				30.14

3.2 Model Validation

A one-dimensional gamma index (see Section 2.2.1) was used to verify that 90% of calculated dose values passed within 10% of measured dose values or 3 mm in the in-field region of dose measurements and within 2 mGy/Gy or 10 mm in the out-of-field region for each validation field profile. Table 3.7 lists the results of the gamma index analysis on validation profiles measured in air, including the maximum and average γ values as calculated using Equation 2.67 as well as the fraction of points receiving a passing γ value of less than or equal to 1. In this table it can be seen that only three of the validation profiles in air passed at 90% of positions studied. The passing profiles represented the reference conditions as well as the in-plane 20x20 cm^2 field size. Deviations from the reference conditions in terms of source to calculation plane distance and aspect ratio resulted in gamma index values greater than one for more than 90% of locations studied in air.

Figure 3.10 shows γ index values versus off-axis position for the 10x10 cm^2 field measured in the cross-plane direction, in air, at an SPD of 110 cm. This field had a passing rate of about 83%, approximately equal to the passing rate for all fields and thus was considered to be a representative case. The solid black line separates the in-field region from the out-of-field

Table 3.7 – Results of one-dimensional gamma index analysis on in-air validation data. List of the maximum and average gamma index value for each validation profile measured in-air with the gamma index criteria of 10% or 3 mm inside of the treatment field and 2 mGy/Gy or 1 cm outside of the treatment field. Also, the fraction of points passing with a gamma value less than or equal to 1 for each profile is listed. The final row lists the maximum, average, and fraction of all in-air measured doses passing the gamma index analysis criteria for all fields studied.

Field Size (cm^2)	SPD (cm)	Profile	$\gamma_{max}(x_m)$	$\bar{\gamma}(x_m)$	Fraction ≤ 1
10x10 *	101.5 *	In-plane	1.58	0.22	0.994
		Cross-plane	1.06	0.33	0.999
	110	In-plane	1.51	0.52	0.781
		Cross-plane	1.26	0.59	0.827
5x20	101.5	In-plane	1.92	0.43	0.880
		Cross-plane	3.17	0.88	0.709
20x5	101.5	In-plane	2.79	0.72	0.734
		Cross-plane	2.66	0.62	0.772
20x20	101.5	In-plane	2.19	0.59	0.920
		Cross-plane	2.44	0.77	0.739
All Fields			3.17	0.52	0.835

region as determined by Equations 2.61 and 2.62 while the dashed line separates passing and failing gamma index magnitudes. From this plot, it can be seen that while a larger number of failing points were located inside of the treatment field, those that failed outside of the treatment field on average had greater γ values, indicating that they were further outside of the agreement criteria. It can also be seen in this plot that the failing γ values were systematically clustered around the near-field region while the far-from-field region passed with gamma values well below 1.

Table 3.8 lists the results of the gamma index analysis on validation profiles measured in water. In this table it can be seen that all square-field validation profiles passed for at least 90% of measured positions. Changes in depth, SSD, and field area with respect to the reference

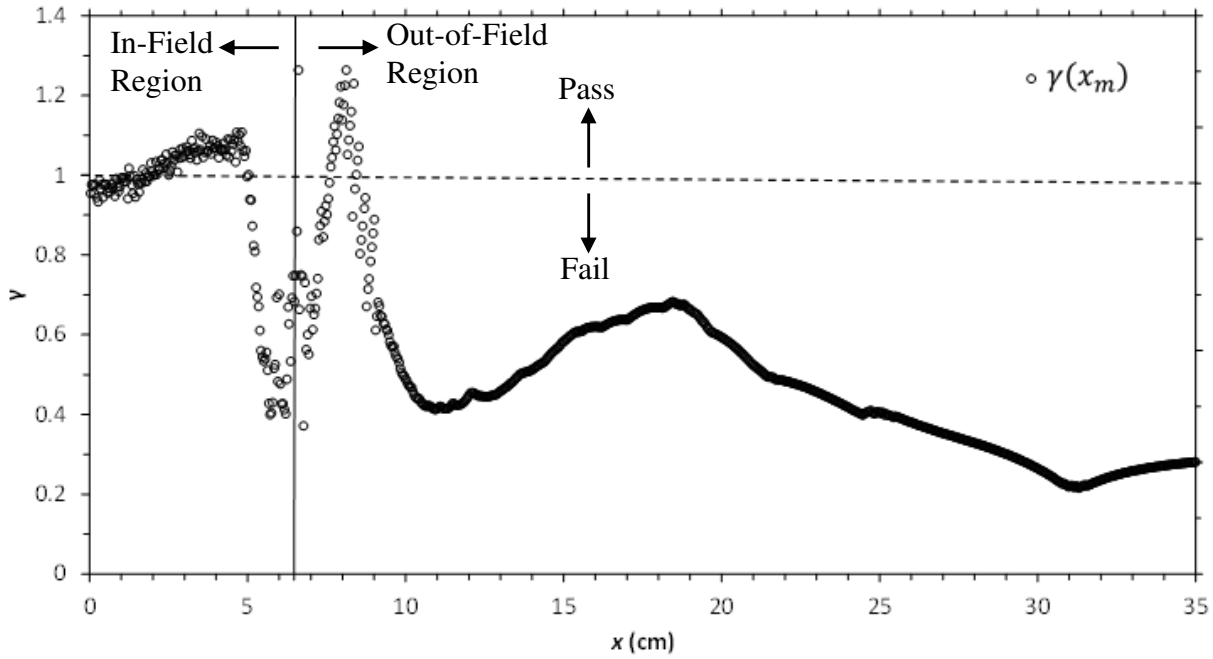

Figure 3.10 – Gamma index versus off-axis position for a representative profile in-air. Plot of the gamma index for each measured position for the 10x10 cm^2 treatment field at an SPD of 110 cm in the cross-plane direction. The vertical line separates points that are defined to be in the treatment field from those considered to be out-of-field based on the criteria described in Section 2.2.1.

conditions of a 10x10 cm^2 field measured at a depth of 1.5 cm in a water-phantom at an SSD of 100 cm were accurately modeled by the algorithm. Deviations from these reference conditions in the aspect ratio generally yielded gamma index results that did not pass for at least 90% of locations studied.

Figure 3.11 shows γ versus off-axis position, x, for the 20x20 cm^2 field measured in the in-plane direction, in a water-phantom at an SSD of 100 cm and with a measurement depth of 1.5 cm. This field had a passing rate of about 92%, approximately equal to the passing rate for all data points and thus was considered to be a representative case. As in Figure 3.10, the solid black line separates the in-field region from the out-of-field region, as determined by Equations 2.61 and 2.62, while the dashed line separates passing and failing gamma index magnitudes.

Table 3.8 – Results of one-dimensional gamma analysis on water-phantom validation data. Table presenting the maximum and average gamma index value for each validation profile measured in water as well as the percentage of total values passing with a gamma value less than or equal to 1. The last row lists the maximum, average, and percentage passing for all in-water measured doses.

Field Size (cm^2)	SSD (cm)	Depth (cm)	Profile	$\gamma_{max}(x_m)$	$\bar{\gamma}(x_m)$	Fraction ≤1
10x10 *	100 *	1.5 *	In-plane	1.50	0.31	0.988
			Cross-plane	1.15	0.30	0.997
	100	10	In-plane	1.57	0.38	0.972
			Cross-plane	1.03	0.34	0.994
5x20	100	1.5	In-plane	0.93	0.26	1.000
			Cross-plane	2.26	0.85	0.778
20x5	100	1.5	In-plane	1.99	0.71	0.835
			Cross-plane	3.08	0.89	0.662
20x20	100	1.5	In-plane	3.42	0.52	0.900
			Cross-plane	2.76	0.48	0.923
10x10	85	1.5	In-plane	2.37	0.38	0.957
			Cross-plane	1.52	0.35	0.971
All Fields				3.42	0.48	0.915

While this plot did have passing gamma index results at greater than 90% of points, it can be seen that those points that did fail were, on average, very far from the agreement criteria. Also, as was the case with the previously discussed in-air profile, the failing points were clustered around the field edge. It should be noted that this is also where the systematic underestimation of dose was observed in Figure 3.9. Unlike the in-air profile in Figure 3.10, the majority of locations inside of the treatment field passed with γ values far lower than 1. It should also be noted that the sharp drop in gamma index magnitude at the location of the black solid line is explained by the change in gamma index criteria at this point as was discussed in Section 2.2.1.

Figure 3.12 shows the fraction of the total absorbed dose represented by each dose component, D_P, D_L, and D_S, as a function of off-axis position. As in the previous two figures, the

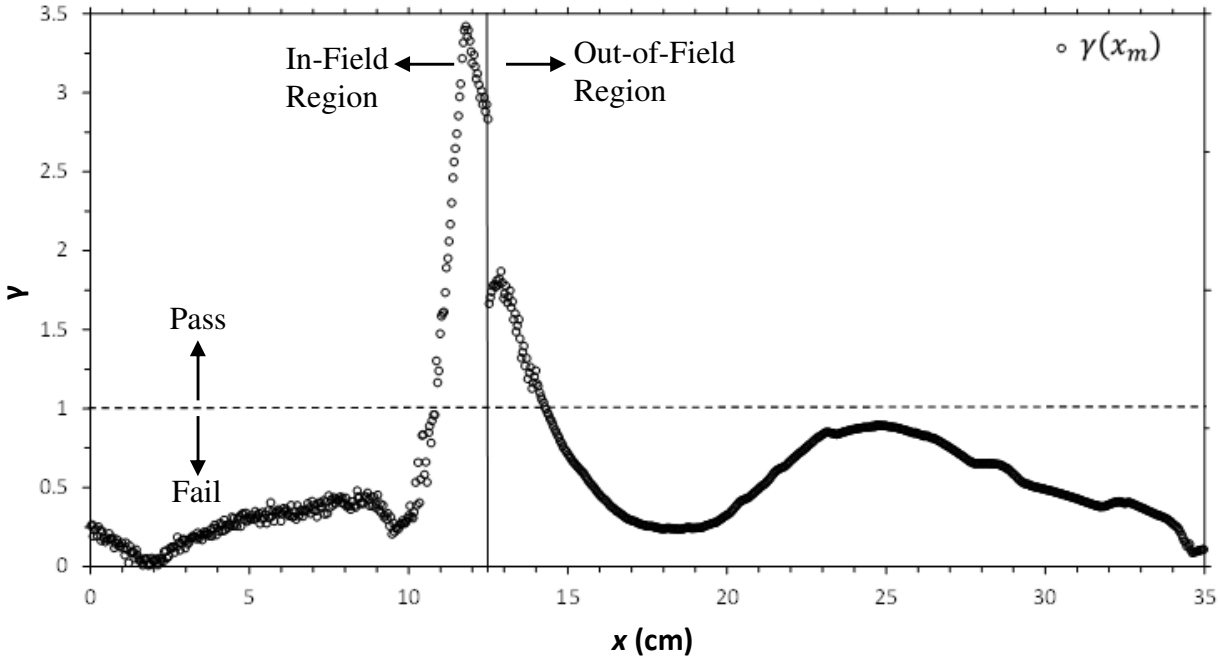

Figure 3.11 - Gamma index versus off-axis position for a representative profile in a water-phantom. Plot of the gamma index calculated for the in-plane measured profile of a 20x20 cm^2 treatment field at an SSD of 100 cm and a measurement depth of 1.5 cm in a water-phantom. The vertical line separates points that are defined to be in the treatment field from those considered to be out-of-field based on the criteria described in Section 2.2.1.

in-field and out-of-field regions are separated by the solid vertical line. From this figure, it can be seen that by far, the largest component of the total dose in the near-field region is from the absorbed dose from scattered photons. This region being where more significant gamma index failures were observed both in air and water-phantom indicates possible shortcomings in the model for scattered dose, which will be explored further in Section 3.3.

3.3 Uncertainty analysis

A rigorous propagation of uncertainties was performed for the developed absorbed dose model following the methods outlined in Section 2.3. This was done in order to independently assess the accuracy of the model. Our analysis of uncertainty in the model of the un-collimated primary photon fluence and the absorbed dose from the collimated fluence, leakage fluence, head-scatter virtual source, and phantom-scatter virtual source in water are presented in Sections

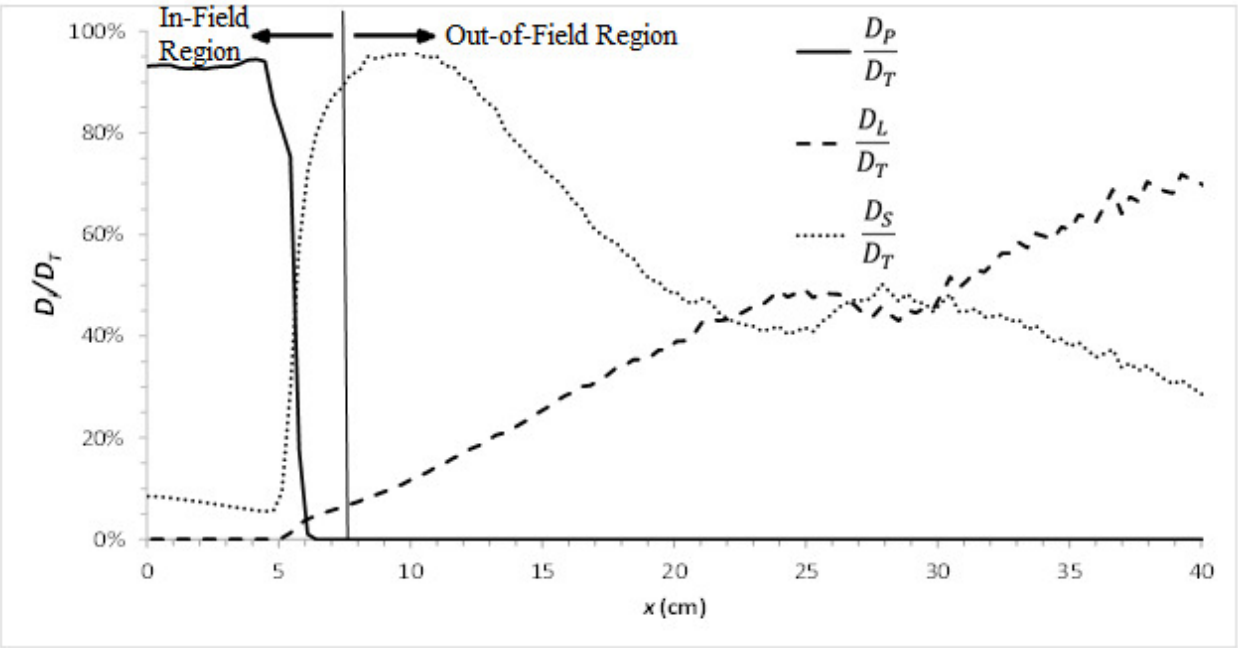

Figure 3.12 – Ratio of each dose component to the total absorbed dose versus off-axis position. Plot of the ratio of each dose component to the total absorbed dose with respect to off axis position for the reference conditions of a 10x10 cm^2 treatment field measured at a depth of 1.5 cm in a water tank at an SSD of 100 cm, scanned in the in-plane direction. The solid vertical line located at 6.5 cm separates the in-field region from the out-of-field region.

3.3.1 through 3.3.5. Finally, in Section 3.3.6, we estimated the uncertainty in the total absorbed dose model.

3.3.1 Uncertainty in Un-Collimated Primary Photon Fluence

In this section we present the results of our estimation of the uncertainty in the un-collimated primary photon fluence model. Table 3.9 lists the relative uncertainty which was estimated for each parameter involved in the model representation of the un-collimated primary photon fluence (see Section 2.1.2).

Table 3.9 – Uncertainty budget for the parameters for un-collimated primary photon fluence.

Symbol	Description	Relative Uncertianty	Source
$\sigma_{\bar{E}}$	Uncertainty in the average beam energy	10%	This Work[14]
$\sigma_{\frac{\mu_{en}}{\rho}}$	Uncertainty in the mass energy absorption coefficient for 2 MeV photons	.01%	This Work[15]
$\sigma_{Y(6MeV)}$	Uncertainty in the photon yield for 6 MeV electrons in tungsten	1%	This Work[16]
$\sigma_{\bar{x}_1}$	Uncertainty in the mean of the central Gaussian	5%	This Work[14]
$\sigma_{\bar{x}_2}$	Uncertainty in the mean of the peripheral Gaussians	10%	This Work[14]
σ_{Q_i}	Uncertainty in the charge of electrons incident on the target producing photons in each Gaussian	10%	This Work[14]
σ_{σ_i}	Uncertainty in the width parameter of each Gaussian	10%	This Work[14]
σ_p	Uncertainty in the exponent driving the divergence of the un-collimated photon fluence	5%	This Work[14]

The uncertainties listed in Table 3.9 were propagated to find the uncertainty in the un-collimated primary photon fluence using Equation 2.68. In order to evaluate this uncertainty at the four discrete locations described in Section 2.3: on the CAX, at the 5% off-axis-ratio position, and at 15 cm and 30 cm off-axis, the uncertainty was calculated for the fluence projected to an SPD of 101.5 cm. The absolute and relative uncertainties at each of these four locations for both the in-plane and cross-plane directions are presented in Table 3.10. From this table it can be seen that the relative uncertainty in the un-collimated primary photon fluence only slightly decreases with off-axis position in both the in-plane and cross-plane direction. Also, while the absolute uncertainty in the un-collimated photon fluence is slightly larger in the cross-plane direction than the in-plane direction at all locations studied, the relative uncertainty is

[14] Estimated
[15] Estimated from (Hubbell & Seltzer, 2011)
[16] Estimated from (Attix, 1986)

lower. This can be explained by the wider profile of the un-collimated photon fluence in the cross-plane direction as depicted in Figure 3.1.

Table 3.10 – Uncertainty in the un-collimated primary photon fluence. List of the uncertainty in the un-collimated primary photon fluence projected to an SPD of 101.5 cm at four off-axis representative locations: on the CAX, at the 5% off-axis ratio position, and at 15 cm and 30 cm from the CAX.

σ_ϕ	CAX	5%	15 cm	30 cm
In-Plane (%)	10.8%	10.8%	10.7%	10.6%
In-Plane (1/cm^2)	1.85×10^6	1.84×10^6	1.83×10^6	1.77×10^6
Cross-Plane (%)	9.48%	9.48%	9.44%	9.30%
Cross-Plane (1/cm^2)	1.95×10^6	1.94×10^6	1.93×10^6	1.87×10^6

3.3.2 Uncertainty in Absorbed Dose from Collimated Primary Photon Fluence

Table 3.11 presents the relative uncertainties estimated for all parameters involved in the model calculation of the absorbed dose in water due to the collimated photon fluence using Equation 2.27. Note that the un-collimated photon fluence appears in this equation and thus, Table 3.11 only includes those additional parameters not already given in Table 3.9.

The uncertainties listed in Table 3.10 and Table 3.11 were used to calculate the uncertainty in the absorbed dose from the collimated photon fluence with Equation 2.70. This uncertainty, evaluated at each of the four locations of interest in both the in-plane and cross-plane directions, is presented in Table 3.12.

The first thing to note from this table is that the absolute uncertainty is 0 mGy/Gy at off-axis positions far outside of the treatment field. This is because the absorbed dose from the collimated photon fluence is defined to be 0 mGy/Gy outside of the treatment field (See Section 2.1.3). Additionally, while the absolute uncertainty falls drastically between the central axis and the 5% off-axis-ratio position, the relative uncertainty is roughly constant. Uncertainties are comparable in the in-plane and cross-plane directions with slightly larger uncertainties found in

Table 3.11 – Uncertainty budget for the parameters involved in calculating the absorbed dose in water from the collimated photon fluence.

Symbol	Description	Relative Uncertainty	Source
$\sigma_{\alpha_{Q_i}}$	Uncertainty in the empirical adjustment parameter for the incident electron charge producing photons in each Gaussian	5%	This Work[17]
$\sigma_{\alpha_{\bar{x}_2}}$	Uncertainty in the empirical adjustment parameter for the mean of each peripheral Gaussian	5%	This Work[17]
$\sigma_{\alpha_{\sigma_i}}$	Uncertainty in the empirical adjustment parameter for the width parameter of central and peripheral Gaussians	5%	This Work[17]
σ_C	Uncertainty in the collimation factor (see Equation 2.24)	5%	This Work[17]
σ_{d_0}	Uncertainty in the distance from the effective photon source to the virtual photon source	5%	This Work[17]
σ_{α_w}	Uncertainty in the empirical adjustment factor to the μt of water	5%	This Work[17]
σ_{μ_w}	Uncertainty in the linear attenuation coefficient of water for 2 MeV photons	0.02%	This Work[18]
σ_d	Uncertainty in the depth in water	5%	This Work[17]
σ_{SSD}	Uncertainty in the source-to-surface-distance	0.3%	This Work[17]
σ_{SDD}	Uncertainty in the source-to-diaphragm-distance	In-Plane: 0.02% Cross-Plane: 0.03%	From Literature[19]

Table 3.12 – Uncertainty in absorbed dose from the collimated primary photon fluence. List of the uncertainty in absorbed dose from the collimated primary photon fluence evaluated at four locations of interest: on the CAX, at the 5% off-axis ratio position, and 15 cm and 30 cm from the CAX.

σ_{D_P}	CAX	5%	15 cm	30 cm
In-Plane (%)	13.9%	13.4%	N/A	N/A
In-Plane (mGy/Gy)	127	1.15	0.00	0.00
Cross-Plane (%)	17.9%	17.2%	N/A	N/A
Cross-Plane (mGy/Gy)	164	1.52	0.00	0.00

[17] Estimated
[18] Estimated from (Hubbell & Seltzer, 2011)
[19] (Elekta Digital Linear Accelerator User Manual, 2007)

the cross-plane direction. This is most likely due to the fact that empirical fit parameters were generally larger in the cross-plane direction than the in-plane direction, resulting in larger absolute uncertainties in these values for the same estimated relative uncertainty.

3.3.3 Uncertainty in Absorbed Dose from Leakage Photon Fluence

Table 3.13 lists the relative uncertainties estimated for all parameters involved in the calculation of absorbed dose from leakage fluence using Equation 2.42. It should be noted that again, the un-collimated photon fluence appears in Equation 2.42, for which the uncertainty was presented in Section 3.3.1. Additionally, some parameters are shared between the models for absorbed dose from collimated fluence and that from leakage fluence, namely μ_w and α_{μ_w}, for which uncertainties were given in Table 3.11.

Table 3.13 – Relative uncertainty in parameters for the absorbed dose from leakage fluence.

Symbol	Description	Relative Uncertainty	Source
σ_A	Uncertainty in the off-axis shape of the un-attenuated leakage fluence	5%	This Work[20]
$\sigma_{\mu_{SC}}$	Uncertainty in the linear attenuation coefficient of the secondary collimator	10%	This Work[20]
$\sigma_{\alpha_{SC}}$	Uncertainty in the empirical adjustment factor to the linear attenuation coefficient of the secondary collimator	5%	This Work[20]
$\sigma_{t_{SC}}$	Uncertainty in the thickness of the secondary collimator	0.009%	This Work[21]
$\sigma_{\mu_{PC}}$	Uncertainty in the linear attenuation coefficient of the primary collimator	15%	This Work[20]
$\sigma_{\alpha_{PC}}$	Uncertainty in the empirical adjustment factor for the linear attenuation coefficient of the primary collimator	5%	This Work[20]
$\sigma_{w_{PC}}$	Uncertainty in the proximal width of the primary collimator	20%	This Work[20]

The uncertainty in absorbed dose from leakage fluence at each of the four locations of interest was calculated using Equation 2.71. The results of these calculations are listed inTable

[20] Estimated
[21] Estimated from (Elekta Digital Linear Accelerator User Manual, 2007)

3.14. In this table it can be seen that the absolute uncertainty in the absorbed dose from leakage fluence is 0 mGy/Gy inside of the treatment field (on the CAX), where the leakage component of the dose is zero by definition. It was found that in both planes, the absolute uncertainty is largest near the field edges and decreases with increasing distance from the CAX. While uncertainties were comparable in the in-plane and cross-plane directions, the cross-plane did have slightly larger magnitudes at every position studied. This is most likely due to the fact that empirical adjustment parameters were generally larger in the cross-plane than in-plane direction.

Table 3.14 – Uncertainty in the absorbed dose from leakage fluence. List of the absolute and relative uncertainty in the absorbed dose from leakage fluence at four off-axis locations of interest: on the CAX, at the 5% off-axis ratio location, and 15 cm and 30 cm from the CAX.

σ_{D_L}	CAX	5%	15 cm	30 cm
In-Plane (%)	N/A	0.0913%	0.0924%	0.0961%
In-Plane (mGy/Gy)	0.00	0.00178	0.00162	0.000654
Cross-Plane (%)	N/A	0.21%	0.209%	0.247%
Cross-Plane (mGy/Gy)	0.00	0.00402	0.00363	0.00219

3.3.4 Uncertainty in Absorbed Dose from the Virtual Source of Head-Scattered Radiation

The estimated relative uncertainty in each parameter involved in the model calculation of absorbed dose from the head-scatter virtual source using Equation 2.52 is presented in Table 3.15. These uncertainties were used with Equation 2.73 to calculate the uncertainty in the absorbed dose from head-scattered photons. This uncertainty was evaluated at four off-axis locations of interest for both the in-plane and cross-plane directions and are given in Table 3.16. First, it should be noted that the absorbed dose from head-scattered photons was found to be negligible far from the treatment field. Thus, relative uncertainty comparisons in this region (i.e. at 15 cm and 30 cm from the CAX) were unrepresentative and have been excluded. In Table 3.16 it can be seen that the absolute uncertainty in the calculated head-scatter dose drastically decreased with off-axis position. The relative uncertainty, on the other hand, showed a much

weaker dependence on distance from the CAX in the region where it could be calculated. Also, the absolute uncertainty in the cross-plane direction revealed a weaker position dependence than that in the in-plane direction. This was expected because the Gaussian shape of the head-scatter absorbed dose profile in the cross-plane direction was characterized by a larger width parameter and thus maintains a larger magnitude further from the CAX than in the in-plane direction.

Table 3.15 – Uncertainty budget for parameters for the absorbed dose from the virtual source of head-scattered radiation.

Symbol	Description	Relative Uncertainty	Source
$\sigma_{\kappa_{HS,FA}}$	Uncertainty in the constant of proportionality for the Gaussian amplitude	10%	This Work[22]
$\sigma_{x_{SC}(0)}$	Uncertainty in the position of the secondary collimator projected to the isocentric plane	0.1%	This Work[23]
σ_u	Uncertainty in the exponent governing the relationship between amplitude and field area	10%	This Work[22]
σ_{SFFD}	Uncertainty in the source-to-flattening-filter-distance	0.06%	This Work[23]
σ_s	Uncertainty in the divergence factor for head-scattered dose	10%	This Work[22]
$\sigma_{\kappa_{HS,\sigma}}$	Uncertainty in the constant of proportionality for the width parameter of the head-scatter Gaussian	5%	This Work[22]
σ_v	Uncertainty in the exponent governing the relationship between the width parameter and field size	10%	This Work[22]
$\sigma_{\alpha_{HS}}$	Uncertainty in the adjustment parameter for the μt of water for head-scattered radiation	5%	This Work[22]

Table 3.16 – Uncertainty in absorbed dose from the virtual source of head-scattered radiation. List of the uncertainty in absorbed dose from the head-scatter virtual source evaluated at 4 off-axis locations of interest: on the CAX, at the 5% off-axis ratio position, and at 15 cm and 30 cm from the CAX, in both the in-plane and cross-plane directions.

$\sigma_{D_{HS}}$	CAX	5%	15 cm	30 cm
In-Plane (%)	172%	145%	N/A	N/A
In-Plane (mGy/Gy)	82.5	36.9	1.09	1.57×10^{-5}
Cross-Plane (%)	187%	169%	N/A	N/A
Cross-Plane (mGy/Gy)	72.8	43.6	5.86	1.82×10^{-2}

[22] Estimated
[23] Estimated from (Elekta Digital Linear Accelerator User Manual, 2007)

3.3.5 Uncertainty in Absorbed Dose from Virtual Source of Phantom-Scattered Radiation

Table 3.17 lists the relative uncertainty budgeted for each parameter involved in the model calculation of absorbed dose due to the phantom-scatter virtual source as calculated using Equation 2.54. The uncertainties listed in Table 3.17 were utilized in Equation 2.74 to calculate the uncertainty in absorbed dose from phantom-scattered photons. This uncertainty was evaluated at four representative off-axis locations of interest. Unlike the previously discussed absorbed dose models, the model for absorbed dose from phantom-scattered photons is the same in the in-plane and cross-plane directions. Instead, parameters were fit independently for changes in depth. Thus, Table 3.18 presents the uncertainty in the phantom-scatter absorbed dose, at each of the four off-axis locations of interest, and for depths of 1.5 cm and 10 cm in water. From this table it can be seen that both the relative and absolute uncertainty decrease with increasing distance from the CAX at both depths studied. However, the uncertainty in the absorbed dose at a depth of 10 cm showed a stronger off-axis position dependence than that at a depth of 1.5 cm. This is most likely because the only phantom-scatter parameter that was fit independently at each depth was C, the partitioning factor between each Gaussian making up the double-Gaussian. This parameter was significantly larger at a depth of 10 cm than 1.5 cm. This means that at the deeper depth, the model was more heavily weighted in the narrow Gaussian, resulting in a generally stronger off-axis dependence in the dose profile at a depth of 10 cm than at 1.5 cm.

Table 3.17 – Uncertainty budget for parameters involved in absorbed dose from the virtual source of phantom-scattered radiation.

Symbol	Description	Relative Uncertainty	Source
$\sigma_{\kappa_{PS,FA}}$	Uncertainty in the constant of proportionality for the double-Gaussian amplitude	10%	This Work[24]
σ_w	Uncertainty in the exponent governing the relationship between amplitude and field area	10%	This Work[24]
σ_b	Uncertainty in the exponent describing the power law relationship between amplitude and depth	10%	This Work[24]
$\sigma_{\kappa_{PS,\sigma,1}}$	Uncertainty in the constant of proportionality for the width parameter of Gaussian 1	5%	This Work[24]
σ_f	Uncertainty in the exponent governing relationship between the width parameter of Gaussian 1 and field size	10%	This Work[24]
$\sigma_{\kappa_{PS,\sigma,2}}$	Uncertainty in the constant of proportionality for the width parameter of Gaussian 2	10%	This Work[24]
σ_h	Uncertainty in the exponent defining the relationship between the width parameter of Gaussian 2 and field area	10%	This Work[24]
σ_C	Uncertainty in the partitioning factor between the two component Gaussians	10%	This Work[24]
$\sigma_{\alpha_{PS,i}}$	Uncertainty in the adjustment parameter to the μx of phantom-scattered radiation in each Gaussian	5%	This Work[24]

Table 3.18 – Uncertainty in the absorbed dose from the virtual source of phantom-scattered radiation. List of the uncertainty in absorbed dose from phantom-scattered photons evaluated at four off-axis locations of interest. Note that presented values apply to both in-plane and cross-plane calculations as the model is shared between the two planes.

$\sigma_{D_{PS}}$	CAX	5%	15 cm	30 cm
d = 1.5 cm (%)	73.2%	59.0%	61.0%	38.9%
d = 1.5 cm (mGy/Gy)	25.0	8.26	1.95	0.274
d = 10 cm (%)	86.9%	67.9%	60.4%	39.0%
d = 10 cm (mGy/Gy)	51.4	13.6	1.26	0.178

3.3.6 Uncertainty in Calculated Total Absorbed Dose

The uncertainties from each dose component presented in Sections 3.3.1 through 3.3.5 were used with Equations 2.69 and 2.72 to determine the uncertainty in the calculated total absorbed dose. Table 3.19 presents the uncertainty in the total absorbed dose evaluated at each of the four representative locations of interest in the in-plane and cross-plane directions.

[24] Estimated

Differences in uncertainty magnitudes between depths of 1.5 cm and 10 cm were found to be negligible and thus, only the uncertainty at a depth of 1.5 cm is presented. From this table, it can be seen that while the absolute uncertainty generally decreases with off-axis position, the relative uncertainty peaks at the 5% off-axis-ratio location. This is consistent with the findings of Specific Aim 2 (See Section 3.2) in that the gamma index analysis revealed that failures in water were largely clustered around this 5% isodose location. By far, the largest contributor to the uncertainty in this region was the absorbed dose from head-scattered photons. It can be seen from Tables 3.16 and 3.19 that the uncertainty in the total absorbed dose is roughly equal to that in the head-scatter dose at both the 5% and 15 cm locations. It was shown in Figure 3.12 that the absorbed dose deposited by scattered photons, of which head-scattered photons are a component, is the largest contributor to the total absorbed dose in this region. Thus, the uncertainty in the total absorbed dose is greatly dependent on the large uncertainties found in this portion of the model. With the exception of the off-axis position of 15 cm, uncertainties were comparable between in-plane and cross-plane directions. The most likely explanation for this difference is the wider width parameter of the head-scatter absorbed dose model in the cross-plane direction. This causes the large uncertainties in this portion of the model to remain important at further off-axis distances while the contribution in the in-plane direction is negligible at the 15 cm location.

Table 3.19 – Uncertainty in the total absorbed dose.

σ_{D_T}	CAX	5%	15 cm	30 cm
In-Plane (%)	15.4%	75.69%	40.8%	19.8%
In-Plane (mGy/Gy)	153	37.8	2.23	0.274
Cross-Plane (%)	18.3%	88.7%	82.9%	17.3%
Cross-Plane (mGy/Gy)	181	44.4	6.18	0.275

Chapter 4 Discussion

A physics-based model was designed to calculate the total absorbed dose deposited both inside and outside of the treatment field for 6 MV photon conventional radiotherapy. The model includes separate terms for absorbed dose from primary, leakage, and scattered photons and was developed to reproduce measured total absorbed dose profiles in a water-box phantom from 6 MV conventional photon radiotherapy. The algorithm was then validated against independently measured profiles in water representing a range of clinically relevant photon field sizes, aspect ratios, off-axis positions, and depths in a water-phantom. The major finding of this study is that validation of the model revealed it was able to predict doses meeting the criteria of passing within 25% or 3 mm of measured doses inside the treatment field and 2 mGy/Gy or 10 mm of measured doses outside of the treatment field at 90% of measured positions for all square fields studied in water.

4.1 Impact

Current treatment planning systems do not include the capability to accurately predict the absorbed dose beyond a few centimeters outside of the treatment field (Taylor & Kron, 2011). This was highlighted by two recent studies (Howell R. M., Scarboro, Kry, & Yaldo, 2010; Joosten, Matzinger, Jeanneret-Sozzi, Bochud, & Moeckli, 2013), and in this work (Section 1.2). Previous to this work, relatively few dose reconstruction algorithms were available. Of those that have been developed, some only attempted to model certain components of the stray dose rather than the total absorbed dose (Benadjaoud, et al., 2012; Chofor, Harder, Willborn, & Poppe, 2012), others were based on measurements from outdated linacs (Stovall, et al., 2006; Francois, Beurtheret, & Dutreix, 1988), and many authors failed to publish even the most basic

aspects of their proposed models (Stovall, et al., 2006; Van der Giessen, 1996; Diallo, et al., 1996).

This work suggests that it is feasible to improve dosimetric accuracy in near-field and out-of-field regions using a simple and computationally fast physics-based analytical algorithm. The potential improvements of out-of-field dose calculations through the use of analytical models is illustrated by Figures 4.1 and 4.2. In Figure 4.1 it can be seen that the treatment planning system significantly underestimates absorbed dose outside a distance of approximately 15 cm from the CAX while the analytical model proposed in this work continues to predict measured doses at greater accuracy out to a distance of 35 cm from the CAX. Figure 4.2 shows the calculated and absorbed dose profiles for a range of different field sizes, depths in phantom, and SSDs. In this figure, it can be seen that the model presented in this work accurately predicts the measured dose values for all of these various field configurations in all regions of the profile.

Absorbed dose calculated using analytical models could prove useful in a number of different applications. The accurate knowledge of absorbed dose deposited outside of the treatment field is especially important for predicting radiation late effects such as second cancer (Newhauser & Durante, 2011), fertility complications (Perez-Andujar, Newhauser, Taddei, Mahajan, & Howell, in press), cardiac toxicity (Zhang, et al., 2011), and other endpoints. One way in which this algorithm could be used is the model in its entirety could be applied to epidemiological and radiation-safety type applications in order to reconstruct absorbed dose for retrospective radiotherapy studies or from radiation accidents. Also, when treating patients with implanted electronic devices, such as defibrillators and pacemakers, the dose to the device must be carefully tracked and kept below 2 Gy for pacemakers and only 1 Gy for defibrillators (Marbach, Sontag, Van Dyk, & Wolbarst, 1994) in order to avoid device malfunction. The

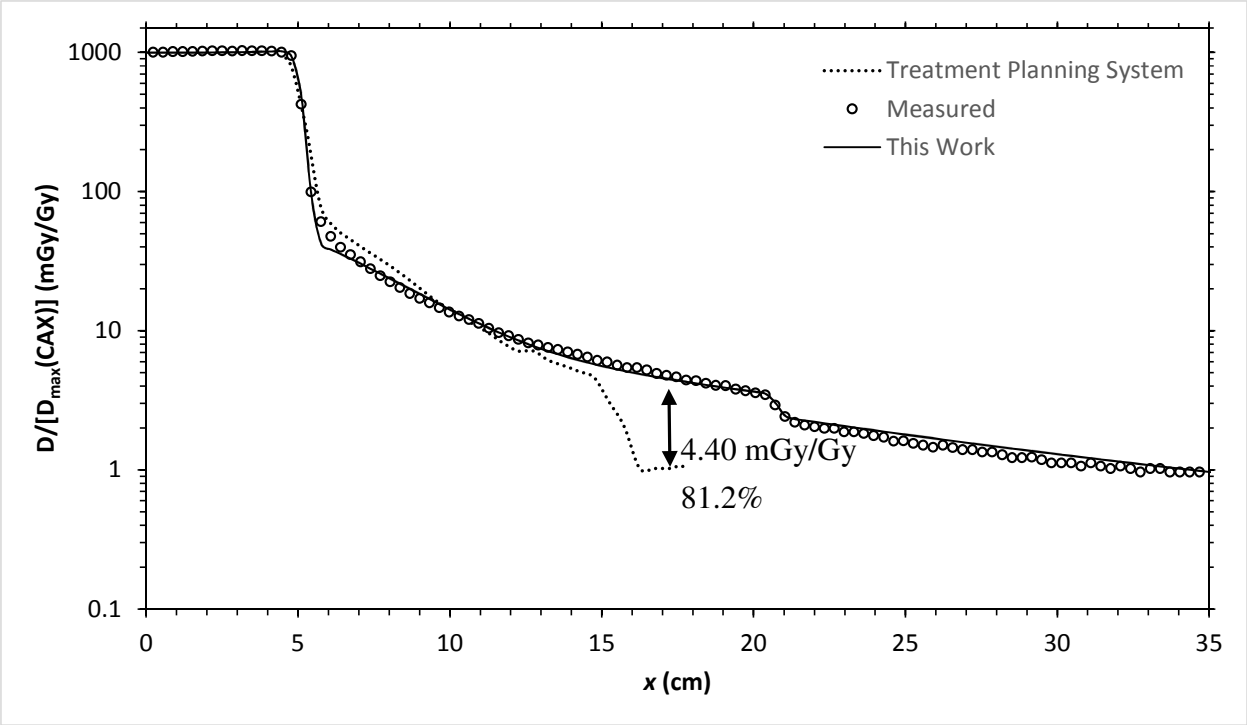

Figure 4.1 – Comparison of measured, TPS calculated, and model calculated total absorbed dose. Plot of the total absorbed dose measured in a water-box phantom with a diamond detector for a 10x10 cm^2 treatment field at a depth of 1.5 cm along with total dose profiles predicted for the same configuration by both a commercial treatment planning system and the analytical model proposed in this work.

model developed in this work could be used as a tool to estimate the expected dose to these devices from radiotherapy treatments. Another possible application is that the out-of-field portion of this model could be integrated into contemporary treatment planning systems in order to improve their current out-of-field dose calculations. For this, the in-field portion of the model would aid in normalization between TPS and model calculated doses. Thus, we conclude that, with additional development, analytical modeling of the total absorbed dose is a viable method of routinely predicting or retrospectively determining the dose delivered both inside and outside of the treatment field during photon radiotherapy treatments.

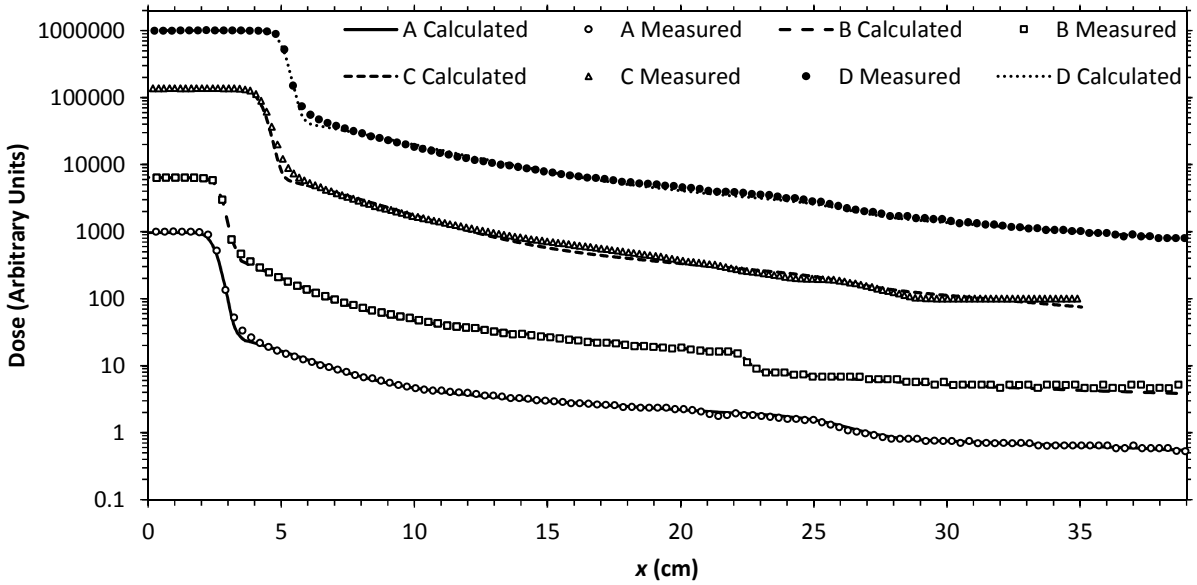

Figure 4.2 – Measured and calculated total absorbed dose for a range of field configurations. Plot of the measured and calculated total absorbed dose for a variety of field configurations. Dose magnitudes have been offset by factors of 10 for visual clarity. A) 5x5 cm^2, d= 1.5 cm, SSD= 100 cm, cross-plane, B) 5x5 cm^2, d= 10 cm, SSD= 100 cm, in-plane, C) 10x10 cm^2, d= 1.5 cm, SSD= 85 cm, cross-plane, D) 10x10 cm^2, d=1.5 cm, SSD= 100, cross-plane.

4.2 Previous Literature

When compared to previous works, the dose algorithm from this study is unique in its ability to calculate total dose both inside and outside of the treatment field. Specifically, this study is the first to consider all major sources of photon fluence in a physics-based analytical model. As a result, direct comparisons of the entire model could not be made with the literature. However, specific aspects of the results could be compared with previous works, specifically those of Kaderka *et al.* (2012), Zhang *et al.* (2011), Taddei *et al.* (in review), Chofor *et al.* (2012), Benadjaourd *et al.* (2012), and Stovall *et al.* (1995).

Kaderka *et al.* (2012) performed out-of-field dose measurements in a water phantom for four different treatment modalities, including 6 MV conventional photon beams. These measurements were used to train the analytical model and thus, agreement between measured profiles from Kaderka *et al.* and calculated absorbed doses from work were detailed in Section

3.1. One of the profiles published in their work, the 10x10 cm^2 treatment field measured at a depth of 1.5 cm in a water-phantom at an SSD of 100 cm, was repeated for the validation portion of this work. Absorbed dose values measured for this work were found to be in good agreement with those published by Kaderka *et al.* as evidenced by an average relative local dose difference of 1.5% inside of the treatment field and 0.4 mGy/Gy in the out-of-field region.

To our knowledge, the first study to attempt to analytically model the total out-of-field absorbed dose was reported by Zhang *et al*. (2011). In this work, total absorbed dose was measured with TLDs in an anthropomorphic phantom and was fit with a double-Gaussian to a distance of 19 cm from the field edge. The in-field portion of the beam was excluded from the model. Following these methods, Taddei *et al.* (in review) developed and tested an analytical model consisting of two gaussians to predict out-of-field dose during craniospinal irradiation using 6 MV photons from two different linacs. Again, the total absorbed dose was measured with TLDs in an anthropomorphic phantom. Unlike this work, in which the double-Gaussian term represents only the dose deposited by phantom-scattered photons, the double-Gaussian in Zhang *et al.* and Taddei *et al.* was used to calculate the total out-of-field absorbed dose. Due to this key difference, direct comparison of model parameters is not possible. However, the general finding of both Zhang *et al.* and Taddei *et al.*, that the out-of-field absorbed dose could be accurately modeled by a simple analytic model consisting of a combination of Gaussians, is in good agreement with this work. In this work, the major components of out-of-field dose, especially in the near-field region, were modeled as a combination of Gaussians, two for the phantom-scatter absorbed dose and one for the head-scatter absorbed dose.

In their work, Chofor *et al.* (2012) considered the dose due to internal scatter, referred to here as “phantom-scatter”. In particular, Chofor *et al.* used Monte Carlo methods to develop an

empirical model to calculate the internal scatter component of dose using a double exponential function however, the manuscript neglected to report the level of agreement between calculated and simulated dose values. Comparison of the model proposed by Chofor *et al.* to the model for absorbed dose from the phantom-scatter virtual source in this work, both calculated for a 5x5 cm^2 treatment field in water, revealed an average dose difference of only 0.15 mGy/Gy. Qualitatively, both models used simple analytical formulas to predict the internal scatter component. However, our results suggest that the double-Gaussian function approach is physically more realistic than the double-exponential due to the discontinuity that arises on the central axis. In this same publication, Chofor *et al.* also studied the energy spectrum of the internally scattered photons. They did not, however, report energy spectra closer to the treatment field than 19.5 cm. Qualitatively they found that the average energy decreased with increasing distance from the treatment field, eventually reaching a value of approximately 500 keV at 25.5 cm from the beam central axis. Our estimates of the linear attenuation coefficient of water for the phantom-scattered photons in the wider Gaussian correspond to an average energy of approximately 400 keV and are therefore in good agreement with this study. Finally, Chofor *et al.* estimated a combined head-scatter and leakage magnitude of 0.3% for a 5x5 cm^2 field, which they assumed was independent of distance from the treatment field. The average combined magnitude of calculated absorbed dose from head-scatter and leakage radiation for a 5x5 cm^2 field from this work was 0.5%, which is in good agreement with the findings of Chofor *et al.*.

Benadjaoud *et al.* (2012) also developed a semi-empirical model for the head-scattered and leakage components of the stray dose. More specifically, they used dose measurements from three different treatment machines to design a multi-plane source model for the head-scatter dose. They reported a median difference in normalized local dose between measurements and

calculations of 9%. The basis of their model matched that of ours, that the total stray dose was equal to the sum of that due to leakage, head-scatter, and phantom-scatter dose. However, unlike this study, Benadjaoud *et al.* did not address the dose due to primary photon fluence, nor did they attempt to model the phantom-scatter portion of the dose. Also, their model for the head-scattered radiation included multi-plane sources located on the edges of the collimation system where as our head-scatter virtual source was located in the flattening filter. Additionally, the model presented by this work was simpler than that of Benadjaoud *et al.*. Due to the complexity of their model, we could not reproduce their results and therefore, a direct comparison of calculated doses was not possible. Both models do, however, include a field size dependence of the head-scatter dose as well as an average photon energy of 2 MeV for a 6 MV photon beam. Benadjaoud *et al.* additionally estimated the magnitude of the leakage dose for 6 MV photon fields at a depth of 10 cm in a water tank, regardless of field size, to a distance of 70 cm from the beam central axis. They reported that the leakage absorbed dose decreased with distance from the field edge and had a magnitude ranging from 0.005% to 0.13%. The corresponding leakage absorbed dose calculated from the model presented in this work ranged from 0.01% to 0.13%. A possible reason for the higher calculated absorbed dose from leakage photons in this work is that the model was only trained and validated to a distance of 40 cm from the CAX while the estimate by Benadjaoud *et al.* extended significantly further from the CAX.

In 1995, the American Association of Physicists in Medicine (AAPM) published Task Group 36 on techniques to estimate and reduce fetal dose from radiotherapy (Stovall, et al., 1995). This report included an appendix presenting out-of-field dose measurements for a range of photon beam energies and depths in the phantom. Measurements were performed in either water or polystyrene using TLD or diode detectors. 6 MV photon beam measurements were

performed on a contemporary linac at the time (Varian Clinac 2100C, Varian Medical Systems, Palo Alto, CA). Figure 4.3 shows this data along with measured and calculated dose values for the same field size from this work. Error bars shown for this work represent one standard deviation conservatively estimated with a 5% relative dose error and .3 mGy/Gy absolute dose uncertainty based on the quantization error. Error bars for Stovall *et al.* (1995) represent one standard deviation estimated based on previously published uncertainty in out-of-field TLD measurements for a 6 MV photon beam (Kry, Price, Followill, Mourtada, & Salehpour, 2007). From this figure it can be seen that the profiles are all in reasonably good agreement with even far-from-field measurements well within uncertainty values. Measurements from Stovall *et al.* outside of 7 cm from the CAX were consistently larger than observed in this work. This is most likely explained by differences in linac head shielding and collimator design between contemporary machines in 1995 and today.

4.3 Study Strengths

This project had several notable strengths. First, it is the first to report a complete, physics-based analytical model to calculate the total dose both inside and outside of the treatment field from photon therapy treatments. To our knowledge it is the only such model that predicts doses due to primary, leakage, and scattered photon fluences for clinically relevant field sizes and depths in the phantom, out to a distance of 40 cm from the CAX. Furthermore, a potentially important advantage of a physics-based approach to modeling absorbed dose, such as the algorithm proposed in this work, is that the model is inherently more readily adaptable to a wide variety of treatment units and treatment techniques than models based on empirical formulae or machine specific lookup-tables, as has been previously available.

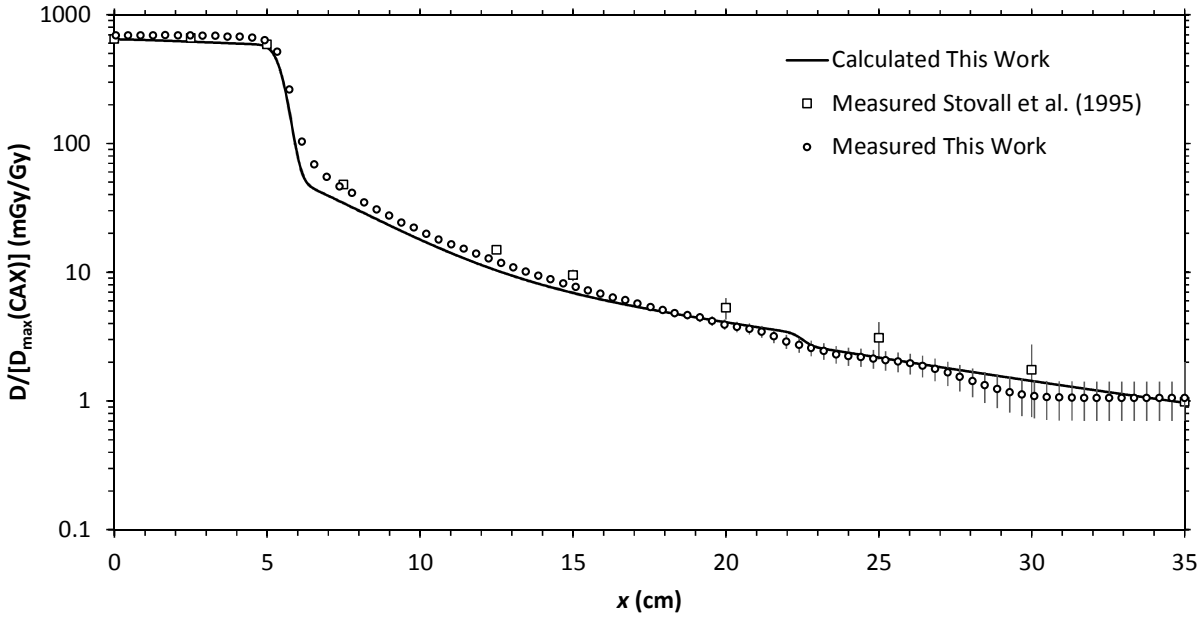

Figure 4.3 – Comparison of this work to Stovall et al. (1995) measurements. All doses measured for a 10x10 cm^2 field of 6 MV photons at a depth of 10 cm in water and normalized to 1000 mGy/Gy at a depth of d_{max} on the central axis.

Additionally, this model was trained and validated using absorbed dose measurements for contemporary radiotherapy treatment units. The majority of previously available models of out-of-field total absorbed dose were developed for equipment that is outdated and the validity of the application of such models to modern linacs is unclear. This work also presented a rigorous uncertainty analysis of the physics-based model, including propagation of errors. Finally, the major strength of this work is that it demonstrated the possibility of the accurate and quick calculation of the dose deposited from 6 MV, conventional photon therapy treatments for both use in epidemiological type studies as well as integration into current treatment planning systems.

4.4 Study Limitations

One limitation of our study is that the in-air training and all validation data was measured using a farmer-type ion chamber. The large volume of this chamber leads to dose averaging in regions of steep dose gradient. This affects the locations of the mean and magnitude of the width

parameter for the Gaussian functions used to model the un-collimated source of photon fluence. This was not a serious limitation because of the inclusion of empirical adjustment parameters determined from small-volume chamber measurements.

A second limitation was that individual dose components were modeled and optimized independently using only total dose measurements. This made it difficult to differentiate between the different components of the total absorbed dose, specifically in the near field region where multiple sources of stray dose are important. While this limitation introduced uncertainty in each independently calculated component of dose, the summation of all components reasonably predicts total absorbed dose in water and thus, the accuracy of this partitioning did not significantly hinder the accuracy of the total absorbed dose model. Furthermore, the use of both in-air and water-tank measurements aided in minimizing these issues.

Another minor limitation is that we estimated the average beam energy to be 1/3 of the peak photon energy based on an assumed triangular photon spectrum. However, it is known that the effects of filtration and beam hardening serve to preferentially remove low energy photons from the beam and thus increase the average beam energy. While this was the best estimate available within the scope of this project, it can be easily overcome with Monte Carlo simulations or measurements.

Validation of the developed model in air revealed that it slightly underestimated absorbed dose far from the treatment field with underestimations increasing in magnitude with field size. However, this underestimation of out-of-field dose was not observed in the validation of the model to water-tank measurements. The only difference between the model in air and water is the additional absorbed dose from phantom-scattered photons. This suggests that some portion of dose that is currently being calculated as phantom-scatter dose, which is only present in water,

is actually due to head-scatter, which is present in both air and water measurements. This indicates the need for further refinement of the head-scatter portion of the model.

Additionally none of the fields studied with aspect ratios other than 1:1 passed the validation criteria. This revealed shortcomings of the model as developed with measured square field data when applied to rectangular fields. However, we believe this limitation may be overcome in a relatively straightforward manner with the inclusion of an additional aspect ratio term in the scatter dose portion of the model.

Finally, the model, as developed, is not expected to apply to IMRT, which is a widely used treatment modality today. However, we believe only minor adjustments would be necessary to include this capability in the current analytical model.

4.5 Future Work

The encouraging results from this study indicate that it may be possible to calculate the total absorbed dose for a variety of field sizes and shapes. However, it appears that the model for absorbed dose from head-scattered photons requires the most immediate attention. A logical next step would be to develop a more detailed characterization of the basic physics relating the head-scatter dose to field size and shape in a simple phantom.

Beyond that, extensions to the model are needed for application to intensity modulated radiotherapy (i.e. IMRT and arc therapies). We believe that similar methods to those used in shielding calculations (NCRP, 2005) could be utilized to this end.

Chapter 5 Conclusions

This work demonstrated that it is possible to calculate the absorbed dose, both inside and outside of a conventional radiotherapy treatment field of 6 MV photons using a physics-based analytical model. This work provided specific results which indicate the use of models, such as the one developed in this project, can predict dose values with better accuracy in the out-of-field region than current treatment planning system methods. This is demonstrated by the agreement between measured and calculated doses within 10% or 3 mm inside of the treatment field and 2 mGy/Gy or 10 mm outside of the treatment field at 90% of positions for all square fields studied in water. Additionally, the average magnitude of local relative deviations between measured and calculated dose values for all in-water validation data was 14%, significantly better than that achievable with contemporary commercial treatment planning systems.

References

Ahnesjo, A. (1989). Collapsed cone convolution of radiant energy for photon dose calculation in heterogeneous media. *Medical Physics, 16*, 577-592.

Attix, F. H. (1986). *Introduction to Radiological Physics and Radiation Dosimetry.* Federal Republic of Germany: Wiley-VCH.

Awotwi-Pratt, J. B., & Spyrou, N. M. (2007). Measurement of photoneutrons in the output of 15 MV varian clinac 2100C LINAC using bubble detectors. *Journal of Radioanalytical and Nuclear Chemistry, 271*(3), 679-684.

Benadjaoud, M. A., Bezin, J., Veres, A., Lefkopoulos, D., Chavaudra, J., Bridier, A., . . . Diallo, I. (2012). A multi-plane source model for out-of-field head scatter dose calculations in external beam photon therapy. *Physics in Medicine and Biology, 57*, 7725-7739.

Chofor, N., Harder, D., Willborn, K. C., & Poppe, B. (2012). Internal scatter, the unavoidable major component of the peripheral dose in photon-beam radiotherapy. *Physics in Medicine and Biology, 57*, 1733-1743.

de Moor, J. S., Mariotto, A. B., Parry, C., Alfano, C. M., Padgett, L., Kent, E. E., . . . Rowland, J. H. (2013). *Cancer Survivors in the United States: Prevalence across the Survivorship Trajectory and Implication for Care.* American Association for Cancer Research.

DeVita, Jr, V. T., Lawrence, T. S., & Rosenberg, S. A. (2008). *Cancer: Principles and Practice of Oncology.* Philadelphia: Lippincott Williams and Wilkins.

Diallo, I., Lamon, A., Shamsadin, A., Grimaud, E., de Vathaire, F., & Chavaudra, J. (1996). Estimation of the radiation dose delivered to any point outside the target volume per patient treated with external beam radiotherapy. *Radiotherapy and Oncology, 38*, 269-271.

Elekta Digital Linear Accelerator User Manual. (2007). Stockholm, Sweden: Elekta Limited.

Francois, P., Beurtheret, C., & Dutreix, A. (1988). Calculation of dose delivered to organs located outside the radiation beams. *Medical Physics, 15*(6), 879-883.

Han, T., Mikell, J. K., Salehpour, M., & Mourtada, F. (2011). Dosimetric compariosn of Acuros XB deterministic radiation transport method with Monte Carlo and model-based convolution methods in heterogeneous media. *Medical Physics, 38*, 2651-2664.

Howell, R. M., Scarboro, S. B., Kry, S. F., & Yaldo, D. Z. (2010). Accuracy of out-of-field dose calculations by a commercial treatment planning system. *Physics in Medicine and Biology, 55*, 6999-7008.

Howell, R. M., Scarboro, S. B., Taddei, P. J., Krishnan, S., Kry, S. F., & Newhauser, W. D. (2010). Methodology for determining doses to in-field, out-of-field, and partially in-field organs for late effects studies in proton therapy. *Physics in Medicine and Biology, 55*, 7009-7023.

Howlader, N., Noone, A. M., Krapcho, M., Neyman, N., Aminou, R., Waldron, W., . . . Freuer, E. J. (2009). *SEER Cancer Statistics Review, 1975-2009 (Vintage 2009 Populations).* Bethesda, MD: National Cancer Institute. Retrieved from http://seer.cancer.gov/csr/1975_2009_pops09/

Hubbell, J. H., & Seltzer, S. M. (2011, December 9). *Tables of X-Ray Mass Attenuation Coefficients and Mass Energy-Absorption Coefficients from 1 keV to 20 MeV for Elemets Z = 1 to 92 and 48 Additional Substances of Dosimetric Interest.* Retrieved from http://www.nist.gov/pml/data/xraycoef/index.cfm

Johns, H. E., & Cunningham, J. R. (1953). *The Physics of Radiology.* Springfield: Charles C. Thomas.

Joosten, A., Matzinger, O., Jeanneret-Sozzi, W., Bochud, F., & Moeckli, R. (2013). 3-dimensional and hybrid intensity modulated radiation therapy for breast cancer based on Monte Carlo and convolution/superposition algorithms: Implications for secondary cancer risk assessment. *Radiotherapy and Oncology, 106*, 33-41.

Kaderka, R., Durante, M., & Kraft, G. (2011). *Out-of-Field Dose Measurements in Radiotherapy.* PhD Thesis , Darmstadt.

Kaderka, R., Schardt, D., Durante, M., Berger, T., Ramm, U., Licher, J., & La Tessa, C. (2012). Out-of-field dose measurements in a water phantom using different radiotherapy modalities. *Physics in Medicine and Biology, 57*, 5059-5074.

Khan, F. M. (2010). *The Physics of Radiation Therapy* (4th ed.). Baltimore, MD: Lippincott Williams and Wilkins.

Kosary, C. L., Ries, L. A., & Miller, B. A. (1995). *SEER Cancer statistics review 1972-1992: tables and graphs.* Bethesda, MD: National Cancer Institute.

Kry, S. F., Price, M., Followill, D., Mourtada, F., & Salehpour, M. (2007). The use of LiF (TLD-100) as an out-of-field dosimeter. *Journal of Applied Clinical Medical Physics, 8*(4).

Low, D. A., Harms, W. B., Mutic, S., & Purdy, J. A. (1998). A technique for the quantitative evaluation of dose distributions. *Medical Physics, 25*(5), 656-661.

Mackie , T. R., Scrimger, J. W., & Battista, J. J. (1985). A convolution method of calculating dose for 15-MV x-rays. *Medical Physics, 12*, 188-196.

Marbach, J. R., Sontag, M. R., Van Dyk, J., & Wolbarst, A. B. (1994). Management of radiation oncology patients with implanted cardiac pacemakers: Report of AAPM Task Group No. 34. *Medical Physics, 21*(1), 85-90.

McKenzie, A. L., & Stevens, P. H. (1993). How is photon head scatter in a linear accelerator related to the concept of a virtual source? *Physics in Medicine and Biology, 38*, 1173-1180.

Mesbahi, A., Fix, M., Allahverdi, M., Grein, E., & Garaati, H. (2005, March). Monte Carlo calculation of Varian 2300C/D Linac photon beam characteristics: a comparison between MCNP4C, GEANT3 and measurements. *Applied Radiation and Isotopes, 62*(3), 467-477.

Mohan, R., Chi, C., & Lidofsky, L. (1986). Differential pencil beam dose computation model for photons. *Medical Physics, 13*, 64-73.

NCRP. (2005). *NCRP Report No. 151: Structural Shielding Design and Evaluation for Megavoltage X- and Gamma-Ray Radiotherapy Facilities.* Bethesda, Maryland: National Council on Radiation Protection and Measurements.

NCRP. (2009). *NCRP Report No. 163: Radiation Dose Reconstruction: Principles and Practices.* Bethesda, MD: National Council on Radiation Protection and Measurements.

Nelms, B. E., & Simon, J. A. (2007). A survey on planar IMRT QA analysis. *Journal of Applied Clinical Medical Physics, 8*(3), 76-90.

Newhauser, W. D., & Durante, M. (2011). Assessing the risk of second malignancies after modern radiotherapy. *Nature Reviews*, 693-703.

Perez-Andujar, A., Newhauser, W. D., Taddei, P. J., Mahajan, A., & Howell, R. M. (in press). Predicted relative risk of follicular depletion for three radiotherapy modalities in a girl receiving craniospinal irradiation. *Physics in Medicine and Biology*.

Smart, D. R. (2010). *Physician Characteristics and Distribution in the U.S.* Chicago, IL: American Medical Association.

Stovall, M., Blackwell, C. R., Cundiff, J., Novack, D. H., Palta, J. R., Wagner, L. K., & Webster, E. W. (1995). Fetal Dose from Radiotherapy with Photon Beams. *Medical Physics, 22*(1), 63-82.

Stovall, M., Weathers, R., Kasper, C., Smith, S. A., Travis, L., Ron, E., & Kleinerman, R. (2006). Dose Reconstruction for Therapeutic and Diagnostic Radiation Exposures: Use in Epidemiological Studies. *Radiation Research, 166*(1), 141-157.

Svensson, R., & Brahme, A. (1996). Effective source size, yield and beam profile from multi-layered bremsstrahlung targets. *Physics in Medicine and Biology, 41*, 1353-1379.

Taddei, P. J., Jalbout, W., Howell, R. M., Khater, N., Geara, F., Homann, K., & Newhauser, W. D. (in review). Analytical model for out-of-field dose in photon craniospinal irradiation.

Taylor, M. L., & Kron, T. (2011). Consideration of the radiation dose delivered away from the treatmnet field to patients in radiotherapy. *Journal of Medical Physics, 36*, 59-71.

Van der Giessen, P. (1996). A simple and generally applicable method to estimate the peripheral dose in radiation teletherapy with high energy x-rays or gamma radiation. *International Journal of Radiation Oncology, Biology, and Physics, 35*(5), 1059-1068.

Zhang, R., Etzel, C., Mahajan, A., Mirkovic, D., Howell, R., & Newhauser, W. (2011). *Quantitative comparison of late effects following photon versus proton external-beam radiation therapies: Toward an evidence-based approach to selecting a treatment modality.* PhD Dissertation.

Vita

Lydia Wilson was born in Winfield, Illinois to Diane Batistich and John Scott Wilson. After falling in love with physics, she graduated from Downers Grove South High School in 2005 and moved to sunny California to attend the University of California, Berkeley where she majored in physics and minored in music. After receiving her Bachelor of Arts in 2009, Lydia spent a year backpacking across Europe and living in Sydney, Australia. During this time, she became interested in the field of medical physics and was admitted to the Master of Science program at Louisiana State University in 2010. During her time in Baton Rouge, Lydia balanced her student life by teaching Zumba Fitness classes and jumping out of airplanes. Lydia is aiming to remain a student as long as humanly possible and will be embarking on another year long adventure as the recipient of a Fulbright Student Fellowship to Croatia where she will research radiotherapy healthcare disparities in the capital city of Zagreb. Upon the conclusion of this fellowship, she will matriculate into the medical physics PhD program at the University of Texas Health Science Center at Houston in the Graduate School of Biomedical Sciences.